RETINAL BLOOD VESSEL IMAGE SEGMENTATION AND CLASSIFICATION OF EPILEPTIC SEIZURE EEG SIGNALS FOR COMPUTER-AIDED DIAGNOSIS

M. Tech. Thesis

By

ASHWANI KUMAR TIWARI

DISCIPLINE OF ELECTRICAL ENGINEERING

INDIAN INSTITUTE OF TECHNOLOGY INDORE

JUNE 2016

RETINAL BLOOD VESSEL IMAGE SEGMENTATION AND CLASSIFICATION OF EPILEPTIC SEIZURE EEG SIGNALS FOR COMPUTER-AIDED DIAGNOSIS

A THESIS

Submitted in partial fulfillment of the
requirements for the award of the degree
of
Master of Technology
in
Electrical Engineering
with specialization in
Communication and Signal Processing

by

ASHWANI KUMAR TIWARI

DISCIPLINE OF ELECTRICAL ENGINEERING
INDIAN INSTITUTE OF TECHNOLOGY INDORE

JUNE 2016

INDIAN INSTITUTE OF TECHNOLOGY INDORE

CANDIDATE'S DECLARATION

I hereby certify that the work which is being presented in the thesis entitled **"Retinal blood vessel image segmentation and classification of epileptic seizure EEG signals for computer-aided diagnosis"** in the partial fulfillment of the requirements for the award of the degree of **MASTER OF TECHNOLOGY** with specialization in **COMMUNICATION AND SIGNAL PROCESSING** and submitted in the **DISCIPLINE OF ELECTRICAL ENGINEERING, Indian Institute of Technology Indore**, is an authentic record of my own work carried out during the time period from MAY 2014 to JUNE 2016 under the supervision of Dr. Ram Bilas Pachori, Associate Professor and Dr. Vivek Kanhangad, Assistant Professor, Discipline of Electrical Engineering.

The matter presented in this thesis has not been submitted by me for the award of any other degree of this or any other institute.

Signature of the student with date
ASHWANI KUMAR TIWARI

This is to certify that the above statement made by the candidate is correct to the best of my knowledge.

Signature of the Supervisor
Dr. RAM BILAS PACHORI

Signature of the Supervisor
Dr. VIVEK KANHANGAD

ASHWANI KUMAR TIWARI has successfully given his M.Tech. Oral Examination held on **3rd June 2016**.

Signature of Supervisors of M.Tech. Thesis
Date:

Convener, DPGC
Date:

Signature of PSPC Member
Date:

Signature of PSPC Member
Date:

ACKNOWLEDGEMENTS

At first I would like to express my sincere gratitude to my supervisors, **Dr. Ram Bilas Pachori and Dr. Vivek Kanhangad** for their encouragement, guidance and support during my post-graduation study and thesis work. They have always been my source of inspiration during my stay at IIT Indore and shall be, all my life.

I would like to thank all the faculty members for teaching me during my course work, which laid a strong foundation which eventually has helped me a lot to pursue further research.

I thank to my seniors Sourabh Solanki and Omkishor Sahu for technical discussions and encouragement, without their continuous cooperation it would have been difficult for me to finish research work within stipulated time.

I am thankful to the entire Signal and Image processing research group for directly or indirectly helping me in completion of my project work. I wish to express my sincere thanks to Prof. B.K. Panigrahi, IIT Delhi for proving EEG dataset and having fruitful discussions during my thesis work.

I am also thankful to all the members of Electrical Engineering research lab for their constant support and guidance.

I would also like to thank all my colleagues for making a wonderful company and having fruitful discussions with me.

I should also mention that without the support of my family members. I could not have accomplished my ambition. Their sacrifices and unbounded love, remind and motivates me to remain determined and focused always pushes me to strive for excellence. I dedicate my M.Tech thesis to my great parents for their countless sacrifices.

Ashwani Kumar Tiwari
M.Tech. (Communication and Signal Processing)
mt1402102003
Discipline of Electrical Engineering
IIT Indore

TABLE OF CONTENTS

LIST OF TABLES

LIST OF FIGURES

Abstract

In the last decade, the use of computer-aided diagnosis (CAD) is greatly promoted and has improved the diagnosis of diseases to great extent. It has potential to assist doctors in taking final decisions with CAD result as a “second opinion”.

Continuous monitoring of Electroencephalogram (EEG) is very cumbersome and may not be possible in some situations, in those places CAD can be a better alternative. This thesis present a new methodology for CAD by finding repetitive local patterns in the biomedical signals. Accuracy of diagnosis depends on how precise abstraction of diseases is captured in these features, and how significant these features are from diagnosis point of view. Recently authors in [1] and [2] experimentally show that diagnosis of certain diseases like epilepsy and diabetes can be achieved by analysing local neighbourhood patterns. A very common example of local pattern is local binary pattern (LBP) which describes local textures, pattern recognition also includes analysis of high level features like Eigen values of hessian matrix like in Frangi vesselness filter. In this work two methodologies are proposed, the first methodology is intended to analyse local pattern in the neighbourhood of retinal image to find correlated structure (i.e. retinal vessels) which in turn segments the retinal blood vessels and is evaluated on two well-studied and different databases DRIVE and STARE. It must me noted that Detection or segmentation of retinal blood vessels greatly helps in identifying vessel abnormalities, which is characteristic of retinal vascular disorders including diabetic retinopathy (DR). The second methodology is developed for detection of local pattern corresponding to seizure that effectively perform classification of epileptic seizure and also is evaluated on two databases. There is a dire need of CAD for detection and classification of epileptic seizure as diagnosis of epilepsy based on the visual inspection of EEG signals can be cumbersome and may take a long time, especially for long-duration EEG signals .The first database is of epilepsy obtained from university of Bonn, it has recordings from patients during epileptic attack and in absence of it. It also has recording from normal persons. The second database is obtained from Sir Ganga Ram Hospital, New Delhi it has recording from patients suffering from epilepsy. The advantage of the both methodologies other

than the very high accuracy, are very low timing complexity that makes these methods well suitable for near real time applications and for devices with limited resources. These advantages makes the proposed methodology well suitable for computer-aided diagnosis of epileptic seizures and segmentation of retinal blood vessels.

Chapter 1
Introduction and literature review

The objective of this study is twofold, the first one is detection and measurement of vessel like structures which are helpful for medical image analysis and diagnosis and the second one is electroencephalogram (EEG) based automated diagnosis of epilepsy. This section briefly presents the importance of vessel segmentation and its application to medical images. It must be noted that as the imaging technology progresses quality of acquired images increases, which eventually increases examination time required in case of computer aided diagnosis (CAD). To process the medical images in timely fashion timing complexity should be as low as possible. Extraction of vessels is the primary step in the CAD analysis the final objective remains extraction of important attributes from fundus images like diameter, length, branching angles or tortuosity of vessel segments. It addition, although in this study vessel extraction is proposed exploiting local neighbourhood properties, but due to generality of proposed methodology it can be applied to other areas of medical imaging. The following section presents the importance of EEG signals for diagnosis of epilepsy.

The EEG signals are commonly used for diagnosis of epilepsy. The proposed method involves detection of key-points at multiple scales in EEG signals using a pyramid of difference of Gaussian (DoG) filtered signals. Local binary patterns (LBP) are computed at these key-points and the histogram of these patterns are considered as the feature set, which is fed to the support vector machine (SVM) for classification of EEG signals. The proposed methodology has been investigated for the four well-known classification problems namely, (i) normal and epileptic seizure, (ii) epileptic seizure and seizure-free, and (iii) normal, epileptic seizure, and seizure-free, (iv) epileptic seizure and non-seizure EEG signals using publically available university of Bonn EEG database. Our experimental results in terms of classification accuracies have been compared with existing methods for classification of the above mentioned problems. Further, performance evaluation on another EEG dataset collected at Sir Ganga Ram

Hospital, New Delhi shows that our approach is effective for classification of seizure and seizure-free EEG signals. The proposed methodology based on LBP computed at key-points is simple and easy to implement for real-time epileptic seizure detection.

The following section briefly presents the existing state-of-the-art methods in the area of vessel segmentation using retinal images and a methodologies for seizure classification using EEG signals.

1.1. Review of vessel segmentation methodologies

In this section an abstract review of the existing vessel segmentation methodologies is presented. Automated segmentation of blood vessels in retinal images is among the most researched topics in the medical image analysis. Detection or segmentation of retinal blood vessels greatly helps in identifying vessel abnormalities, which is characteristic of retinal vascular disorders including diabetic retinopathy (DR). Diabetes is a global health issue and long-term diabetic condition leads to health complications including DR, which has emerged as one of the major causes of vision loss in developed as well as developing countries [3]. According to the study reported in [4], the increase in the number of diabetic patients is alarmingly high and is estimated to be 366 million by the year 2030. Diagnosis and treatment is the key to prevention of vision loss from DR. Therefore, retinal vessel segmentation for detection of vascular abnormalities is an important component in computer aided diagnosis (CAD) using fundus images. Detection of veins and subsequent extraction of their attributes can also be utilized to assess the severity of retinal vascular disorders [5]. Apart from the biomedical applications, features extracted from retinal vessel pattern have also been explored for biometric recognition [6], [7].

Detection of slender veins, which may represent proliferation of new abnormal blood vessels, is one of the major challenges in retinal blood vessel segmentation. Some of these new vessels have been found to be of width as low as one pixel in the acquired fundus images [8]. These slender veins are often lost in the detection process, leading to low true positive rate (TPR). In addition, accurate detection of vessels around the macula is also a major challenge due to low contrast in the region. On the other hand, edges of different structures and patches in fundus images are often incorrectly classified as vessel pixels, leading to high false positive rate (FPR). These structures

are caused by retinal disorders such as macular degeneration and diabetic retinopathy [8].

Retinal vessel segmentation is essentially a binary classification problem, in which each pixel is classified into one of the two classes: blood vessel and non-blood vessel pixels. Over the years, several approaches have been developed to address this problem [9]-[27]. Broadly, retinal vessel segmentation techniques in the literature can be classified into two categories, namely, supervised methods [9]-[15] that require labelled training data and unsupervised methods [16]-[26] that do not require any prior information on the category of pixels. A major drawback of the supervised pixel classification techniques is the requirement of training images with expert annotations. In addition, insufficient number of training images leads to poor classification performance on the test dataset. More importantly, the performance of a supervised method trained on one dataset often deteriorates when evaluated on another dataset [9]. Recently, Zhao et al. [17] developed an infinite active contour model based retinal vessel segmentation approach. The approach utilizes local phase based enhancement filter to obtain more reliable estimate of vesselness and potential outliers are excluded using intensity information of the image.

Roychowdhury et al. [25] proposed an iterative algorithm for vessel segmentation. In each iteration, new vessel pixels are extracted from residual image using an adaptive threshold. The iteration stops when number of false pixels exceeds true vessels pixels in the newly added vessel pixels. However the algorithm requires one time training on the dataset to derive adaptive thresholding function. Imani et al. [26] developed an algorithm for vessel extraction using morphological component analysis (MCA). MCA relies on sparse representation of signals. Lesions are separated from blood vessels using MCA algorithm with the appropriate transforms. Subsequently, final vessel structure is obtained by performing adaptive thresholding on vessel enhanced image generated using Morlet wavelet transform. In general, performance of retinal vessel detection often deteriorates in regions of low contrast and has poor sensitivity for thin vessels [9, 28]. For example, it has been observed that the detection rate of the algorithm based on “Ribbon of Twins” active contour model [28] drops for vessels having width less than three pixels. In addition, central reflex introduces a gap at the center of vessels in the segmented vessel image, as in Staal et al. [10] and Soares et al. [12]. These issues are also discussed by Nguyen et al. [24]. Computational performance of the vessel detection algorithms is another concern,

especially for applications that are expected to run on portable devices [29] with limited computational resources. The above issues motivated us to develop a computationally simpler technique without compromising on the detection accuracy. The following section discusses the existing methodologies for seizure classification using EEG signals.

1.2. Review of seizure classification methodologies

The EEG signals are generally used for diagnosis of epilepsy which affects nearly 50 million persons around the world [30]. Diagnosis of epilepsy based on the visual inspection of EEG signals can be cumbersome and may take a long time, especially for long-duration EEG signals. The advanced signal processing technique based methods may be more suitable for fast, reliable and automatic diagnosis of epilepsy from EEG signals. In the literature, a lot of work has been done using various signal processing techniques in order to determine features for analysis, classification, and detection of epileptic seizures from EEG signals [30], [31].

The signal processing based methods for automated diagnosis of epilepsy which work in time and frequency-domains have been proposed in the literature. For example, the linear prediction model based energy of EEG signals has been explored for the classification of epileptic seizures in [32]. This method exploits the time-domain features like spikes and amplitude of the signal for epileptic seizure detection using EEG. The fractional calculus based more robust linear prediction method has been proposed for classification of epileptic seizure EEG signals in [33]. In this method, the fractional linear prediction model based error energy and energy computations of EEG signals together with support vector machine (SVM) has been suggested for automated classification of epileptic seizure EEG signals. Artificial neural network (ANN) classifier utilizes these features for classification of normal and epileptic seizure EEG signals. The ANN classifier is also used with principal component analysis (PCA) based approach for classification of epileptic seizure EEG signals for diagnosis of epilepsy [34].The local binary pattern (LBP) has been suggested for classification of epileptic seizure EEG signals [1]. In another work, the LBP of the signals decomposed using Gabor filter bank along with the nearest neighbor classifier have been suggested for classification of seizure-free and seizure EEG signals [35].

Another category of approaches for automated diagnosis of epilepsy using EEG signals is based on time-frequency domain and non-stationary signal decomposition techniques. Features based on the time-frequency distributions such as Cohen's class and short-time Fourier transform (STFT) have been proposed in [36]. The ANN classifier utilizes these features for classification of epileptic seizure from EEG signals. Acharya et al. [37] developed an approach for automated diagnosis of epilepsy using higher order spectra (HOS) and texture features from continuous time wavelet transform plot of the EEG signals. In another work, authors employed wavelet transform for obtaining sub-bands of EEG signals and several statistical features of these sub-bands are then computed. For dimensionality reduction of the resulting feature set, authors explored PCA, independent component analysis (ICA) and linear discriminate analysis (LDA). This reduced feature set has been used for the classification of epileptic seizures from EEG signals [38]. The improved forms of generalized fractal dimensions and discrete wavelet transform based methodology has been presented in [39] for epileptic seizure detection.

In another category of approaches that exploit non-linear and non-stationary behaviour of EEG signals, several features computed from the intrinsic mode functions (IMFs) such as the area of phase space representation [40], area of second-order difference plot (SODP) [41], bandwidths of amplitude modulation and frequency modulation [42], area of analytic signal representation (ASR) and instantaneous area [43, 44], combination of area of ASR and area of SODP have been proposed for analysis and classification of epileptic seizure EEG signals [45].

Recurrence quantification analysis [46], Hurst exponent [47], HOS [48], approximate entropy [49] are some of the nonlinear features that have been proposed for automatic detection of epileptic seizures in EEG signals.

1.3. Contribution in this work

Major contributions of the work presented in this thesis are four-fold. Firstly, we propose a new approach for retinal vessel segmentation using eigenvalue maps, which are generated by eigenvalue decomposition of a local covariance matrix. The local covariance matrix is formed by second order image moments. Secondly, a simple approach for detection of centerline vessel pixels is proposed. Detected centerline pixels are further utilized to refine vessel structure obtained using eigenvalue maps.

Comparative experimental evaluation on two benchmark datasets indicates that the performance of the proposed method is quite comparable to recently proposed approaches in this area. Second contribution of this work is a methodology for vessel width estimation. Experimental evaluations on a benchmark dataset indicate that the standard deviation of measurement error in width measurement remains under 1 pixel on all four subsets. Another key advantage of our approach is its computational efficiency.

The final contribution presented in this work is a new method for automated diagnosis of epilepsy using EEG signals. The key feature of our approach is that it involves computation of LBP only at a set of stable key-points, which are detected through a multi-scale analysis of the EEG signal. In contrast to this, the conventional LBP based methods for EEG signal classification [1], [35] compute LBP at every sample value of the EEG signal. As our experimental results indicate, the proposed approach results in significant improvement in performance due to increased discriminating ability of the LBP based feature set when computed at key-points.

1.4. Organization of the work

Rest of the thesis is organized as follows. In chapter 2 a methodology for vessel extraction is proposed. Section 2.1 details the detection of centreline pixels. In Section 2.2.1 and 2.2.2, generation of eigenvalue maps is discussed. Selective growing of centerline pixels is explained in Section 2.2.3. Retinal vessel extraction and post-processing involved are detailed in Section 2.2.4 and 2.3, respectively. An approach for measurement of vessel width is presented in Section 2.4. Chapter 3 presents the detail of the proposed methodology for seizure classification. Specifically, In Section 3.1, details of the approach employed for detection of key-points in EEG signals are presented. Computation of LBP at these key-points and subsequent generation of the feature set, and classifier involved are described in Section 3.2. Chapter 4 describes databases used for performance evaluation, followed by experimental results and discussion. Finally, Chapter 5 presents concluding remarks.

Chapter 2

Proposed methodology for retinal vessel image segmentation

A Framework of the proposed approach for retinal vessel segmentation is shown in Fig. 2.1.

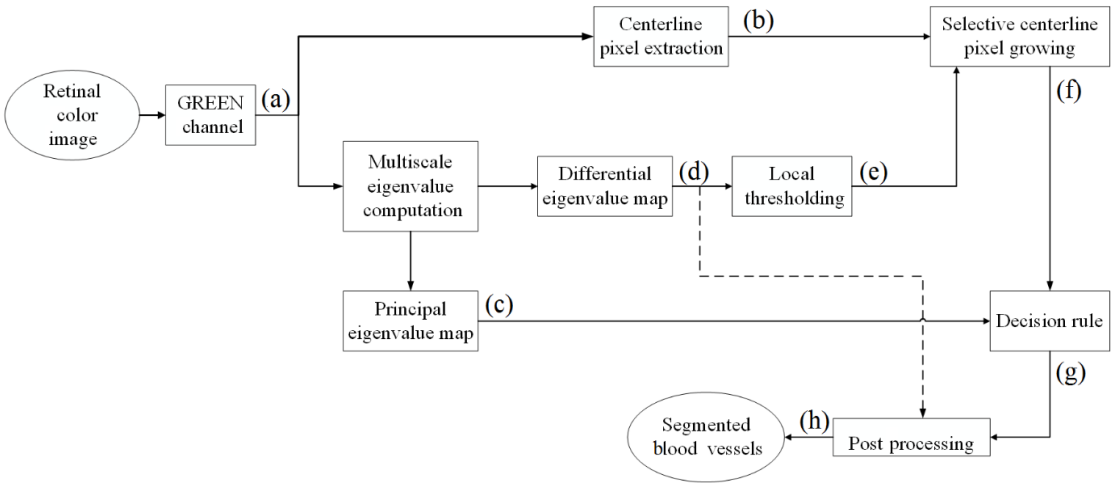

Fig. 2.1. The block diagram of proposed algorithm for blood vessel segmentation.

At first, the green channel of the retinal colour is separated for further processing, as it is realized that green channel shows essentially higher contrast between veins and the background when contrasted with red and blue channels [9], [16], and [20]. The green channel thus separated is handled with a goal to recognize potential candidates for centerline vessel pixels. In particular, centerline pixels are extricated from Gaussian filtered green channel utilizing directional structuring elements. Gaussian filtering is utilized to minimize the impact of noise, however low pass filtering causes obscured vessel boundaries and loss of most slender vessels [9]. In this manner, Gaussian window of size 5×5 is utilized which reduces noise while protecting most slender vessels. At the same time, green channel picture is likewise handled to get a principal eigenvalue map and a differential eigenvalue map using PCA in the neighborhood of every pixel.

A selective vessel growing is performed on extracted centerline pixels with the goal to link pixels corresponding of same vessel segment. The eigenvalue map is normalized and vessel pixels are extracted using simple thresholding. To further improve the performance of vessel detection, falsely detected vessel pixels are removed based on a decision rule taking linked centerline pixels into consideration. Detailed descriptions of the above processing steps are provided in the following sections. A graphical representation of the discussion (including intermediate results) presented in this section is shown in the Fig. 2.2.

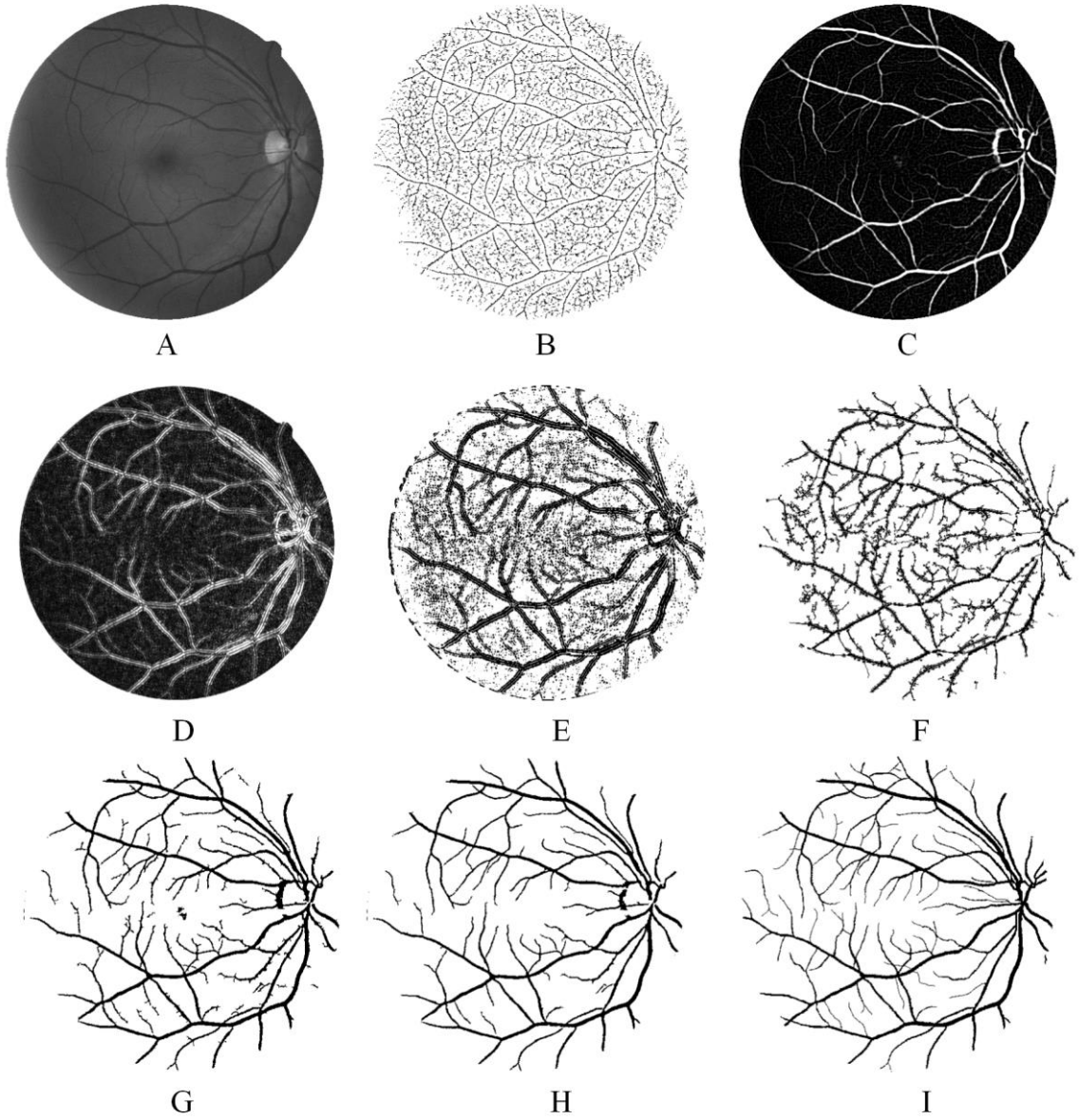

Fig. 2.2 Graphical representation of the proposed methodology: (A) A sample image from DRIVE database; (B) Detected centerline image (after combining all four centerline images); (C) Principal eigenvalue map (contras enhanced for better visualization); (D) Differential eigenvalue map; (E) Thresholded differential eigenvalue map; (F) Segmentation result after performing selective region growing on centerline image; (G) Restoring to original width (obtained from thresholded principal eigenvalue map); (H) Segmented retinal vessel after post-processing; (I) Ground truth segmentation.

2.1 Detection of centreline pixels

This section presents the details of proposed technique for precisely locating centreline pixels. Centerline pixels are characterized as pixels which lies exactly at the center of a vessel segment. It can be seen from Fig. 2.3 centerline vessel pixel represent the nearby minima points on the surface when the retinal image is viewed as a surface in 3D space. Author in [50] showed that profile of a retinal vessels follows Gaussian nature. More precisely the vessel profile when viewed in direction perpendicular to it follows inverted Gaussian with minimum at center. In this work, we developed simple yet proficient method using a set of structuring elements to identify all possible centerline pixels. Specifically, we utilized structuring elements having 7 pixels and oriented along horizontal, vertical and the two diagonal directions, namely 45 and -45 degree. The in-depth details of the proposed centerline detection approach are provided in the following algorithm.

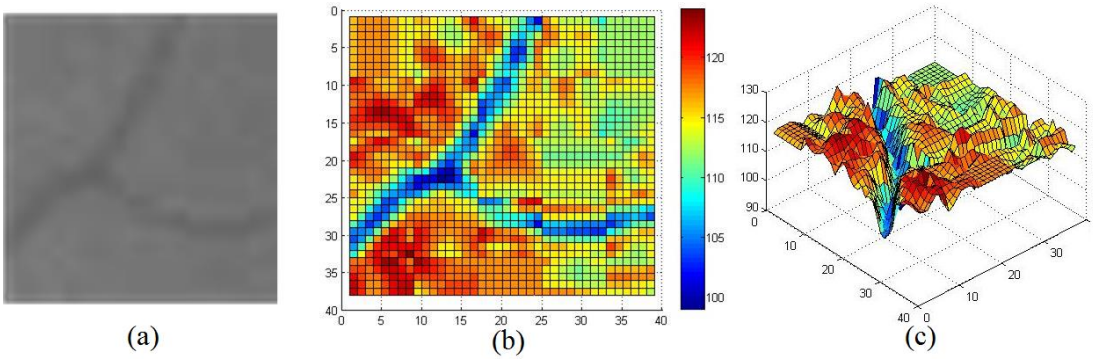

Fig. 2.3. Centerline vessel pixels: (a) A zoomed-in version of a small region of a retinal image containing blood vessels; (b) image in (a) color coded for better representation depicting the fact that centerline pixels represent local minima; (c) image in (a) as a surface in 3D space

---

Algorithm 1: Centerline vessel detection

Input: Gaussian filtered green channel
Output: Extracted centerline vessels
Initialize: Counter $(x, y) = 0$.

For every pixel in the image
For each directional structuring element
Find minima within the probing window. Say (x, y) is the location of the minima, then Counter (x, y)= Counter (x, y)+1;
End
End

At first, the counter is set to zero and the green channel is masked using 4 distinctive structuring elements (SEs), every detecting vessels arranged along a particular

direction. In particular, vessel structures oriented vertically are identified using the horizontally aligned SE, and veins oriented along 45 degree are recognized by the structuring elements directed along - 45 degree. Each pixel is examined using SEs with objective of finding the position of the minima inside probing window and the counter is increased by one at the indices corresponding to the minima location. This process yields a binary image, which is obtained by setting pixel value to 1 if the counter (x, y) value equals to 7. The probing operation is depicted in Fig. 2.4.

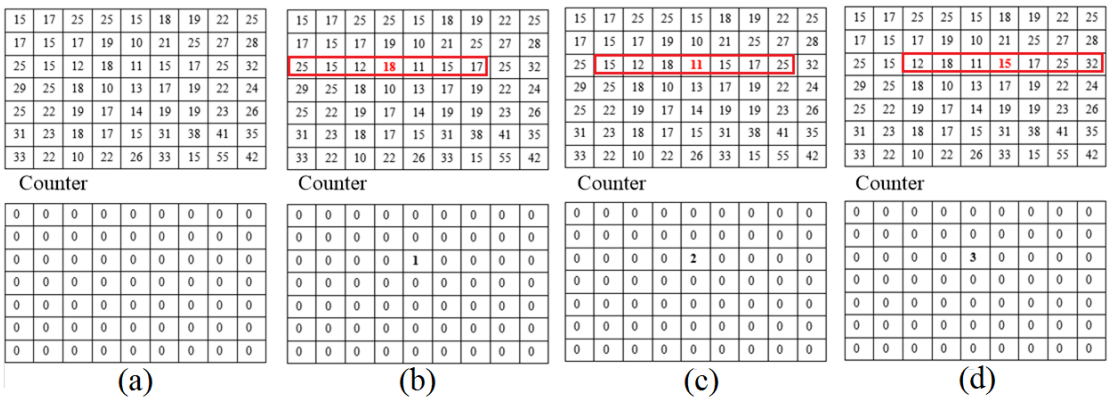

Fig. 2.4. Demonstration of centerline pixel extraction process using horizontal probing window (Pixel being processed is shown in red).

The proposed centerline extraction methodology guarantees that pixels belonging to the same vessel segment are either associated together or are isolated by just a couple of pixels (typically, 1 to 3 pixels) and pixels belonging to various segments are well isolated (at the most 7 pixels). The extracted skeleton of centerline vessels is utilized in removing pathologies to great degree as pathologies don't form any lengthened structures. As can be seen in Fig. 2.5, the procedure portrayed above adequately distinguishes vessel centerline pixels. However, the proposed approach additionally brings about significant number of falsely identified background (non-vessel) pixels. Majority of these erroneously detected non-vessel pixels are excluded from the

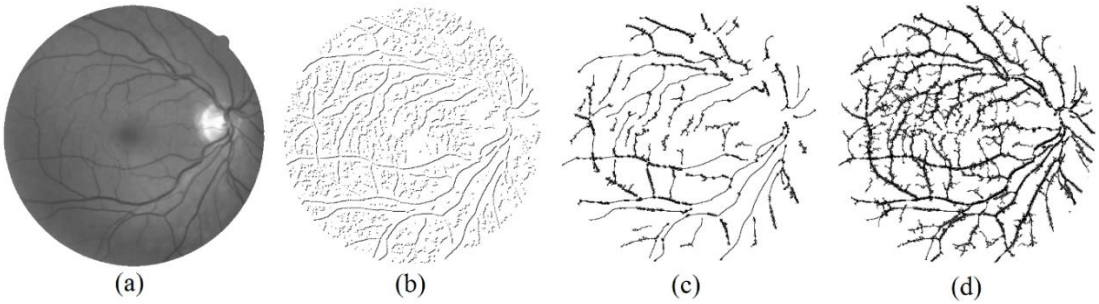

Fig. 2.5. Effectiveness of centerline vessel detection in segmenting single pixel wide blood vessels as well as vessels in poor contrast region: (a) Retinal image; (b) Centerline vessel pixels extracted using -45 degree probing window; (c) Centerline vessels obtained after performing selective region growing on (b) and subsequently removing isolated structures; (d) Final vessel structure obtained by combining individual results of structuring elements oriented in four directions.

principle retinal vessel structure as they does not form extended structures. Therefore, these isolated small structures are removed by imposing minimum bounding rectangle constraint, details of which are provided in Section 2.2.3. However, small fraction of the true vessels also exhibit as separate structure in the centerline vessel image and might get filtered by the bouncing rectangle constraint. Hence, a selective region growing of these centerline pixels is performed to connect small disconnected structures before applying bounding box constraint. The selective region growing approach developed in this work uses the differential eigenvalue map obtained from local PCA. The details of this approach are given in the following section.

2.2. Local principal component analysis

This section present details of the approach developed to segment retinal blood vessels by removing background (non-vessel pixels). The approach make use of PCA applied on local neighborhood (which we refer to as local PCA) of every pixel in the retinal image. This outcomes in higher eigenvalues if the neighborhood pixels are profoundly organized as in case of vessel pixels, which follows inverted gaussian nature. Regions containing background pixels including pathologies in the retinal picture yield lower eigenvalues. In general, for a dataset arranged in a matrix Y of $m \times n$ dimension, the objective of PCA is to discover orthonormal transformation matrix P in equation $Y = PX$ such that covariance matrix $C_y = \frac{1}{n} YY^T$ is a diagonal matrix. The rows of P are the principal components of covariance matrix of X [51].

In this work, the PCA is performed on a covariance matrix, which is formulated using a set of second order image moments [52]. Image moments are computed as the weighted average of pixel intensities in the local neighborhood of a pixel. Kernels involved in the implementation of local PCA on 5×5 neighborhood of a pixel are shown in Fig. 2.6.

Let $I_{x,y}$ be the green channel of the retinal image, the second order moments involved in formulation of the covariance matrix are computed as follows:

$$X_{x,y}^{\text{var}} = \sum_{u=1}^{u=5} \sum_{v=1}^{v=5} (K_{u,v}^{\text{xcentroid}} - X_{x,y}^{\text{centroid}})^2 . I_{x+u-2,y+v-2} \quad (1)$$

$$Y_{x,y}^{\text{var}} = \sum_{u=1}^{u=5} \sum_{v=1}^{v=5} (K_{u,v}^{\text{ycentroid}} - Y_{x,y}^{\text{centroid}})^2 . I_{x+u-2,y+v-2} \quad (2)$$

$$Cov_{x,y} = \sum_{u=1}^{u=5} \sum_{v=1}^{v=5} \left(K_{u,v}^{\text{xcentroid}} - X_{x,y}^{\text{centroid}}\right) . \left(K_{u,v}^{\text{ycentroid}} - Y_{x,y}^{\text{centroid}}\right) . I_{x+u-2,y+v-2} \quad (3)$$

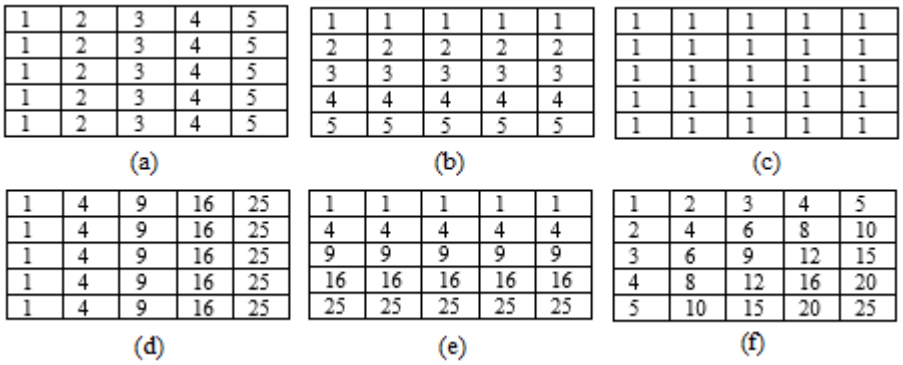

Fig. 2.6. (a) Kernel ($\boldsymbol{K}^{\text{xcentroid}}$) for calculating x component of the centroid; (b) Kernel ($\boldsymbol{K}^{\text{ycentroid}}$) for y component of the centroid; (c) All-one matrix (U); (d) Kernel ($\boldsymbol{K}^{\text{xvar}}$) for calculating x variance (e) Kernel ($\boldsymbol{K}^{\text{yvar}}$) for calculating y variance (f) Kernel ($\mathbf{K}^{\text{cov}}$) for calculating the covariance

where,

$$X_{x,y}^{\text{centroid}} = \frac{\sum_{u=1}^{u=5}\sum_{v=1}^{v=5}(K_{u,v}^{\text{xcentroid}} . I_{x+u-2,y+v-2})}{\sum_{u=1}^{u=5}\sum_{v=1}^{v=5}(I_{x+u-2,y+v-2})} \quad (4)$$

$$Y_{x,y}^{\text{centroid}} = \frac{\sum_{u=1}^{u=5}\sum_{v=1}^{v=5}(K_{u,v}^{\text{ycentroid}} . I_{x+u-2,y+v-2})}{\sum_{u=1}^{u=5}\sum_{v=1}^{v=5}(I_{x+u-2,y+v-2})} \quad (5)$$

Equations (4) and (5) represent X and Y coordinates of the centroid computed for a local neighborhood of a pixel located at (x, y). The local covariance matrix is then computed as follows:

$$\text{Cov}[I_{x,y}] = \begin{bmatrix} X_{x,y}^{\text{var}} & \text{Cov}_{x,y} \\ \text{Cov}_{x,y} & Y_{x,y}^{\text{var}} \end{bmatrix} \quad (6)$$

Eigenvalue decomposition of the above covariance matrix yields two eigenvalues, which are used in our approach to extract the retinal vessel structure. Computation of the covariance matrix and subsequent eigenvalue decomposition is performed for every pixel in the retinal image to obtain eigenvalue maps. However, performing local PCA in comprehensive way as depicted above increases computational complexity and prompts higher memory requirements. To overcome these issues, a fast version is derived by defining calculation of second order moments as matrix algebra, as matrix manipulation is faster in calculation. In particular, the above equations (1)-(5) are expressed in the image correlation form as presented below:

$$X^{\text{var}} = K^{\text{xvar}} * I - (X^{\text{centroid}})^2 \times (U_{5\times5} * I) \quad (7)$$

$$Y^{\text{var}} = K^{\text{yvar}} * I - (Y^{\text{centroid}})^2 \times (U_{5\times5} * I) \quad (8)$$

$$\text{Cov}_{x,y} = K^{\text{cov}} * I - X^{\text{centroid}} \times Y^{\text{centroid}} \times (U_{5\times5} * I) \quad (9)$$

where

$$Y^{\text{centroid}} = \frac{K^{\text{ycentroid}} * I}{U_{5\times5} * I} \tag{10}$$

$$X^{\text{centroid}} = \frac{K^{\text{xcentroid}} * I}{U_{5\times5} * I} \tag{11}$$

$$K^{\text{xvar}} = (K^{\text{xcentroid}})^2 \tag{12}$$

$$K^{\text{yvar}} = (K^{\text{ycentroid}})^2 \tag{13}$$

$$K^{\text{cov}} = K^{\text{xcentroid}} \times K^{\text{ycentroid}} \tag{14}$$

and $U_{5\times5}$ is all-ones matrix of 5×5 elements. In the above equations, I is the green channel of retinal image, $\times$ represents the operation involving multiplication of corresponding elements and $*$ is the image correlation operator. Dimensions of matrices computed using equations (7)-(11) are same as that of the original retinal image.

2.2.1. Eigenvalue map

As described in the previous section, calculation of the covariance matrix and consequent eigenvalue decomposition results in two eigenvalues (principal and second eigenvalue) for each pixel. Fig. 2.7 demonstrates the steps involved in calculation of eigenvalue maps. This procedure produces two eigenvalue maps, in particular principal eigenvalue map and differential eigenvalue map. The principal eigenvalue map is produced utilizing normalized primary eigenvalues, which are obtained by computing the ratio of principal eigenvalue to the pixel value around which the nearby neighborhood is considered.

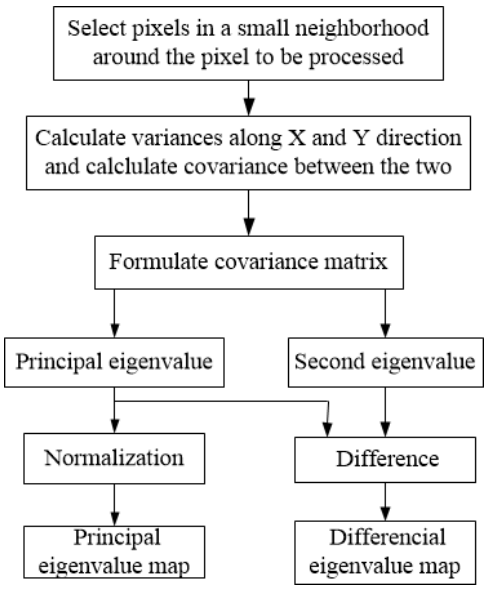

Fig. 2.7. Flow diagram showing generation of principal and differential eigenvalue maps

The major advantage of considering normalized eigenvalue is that it helps in restricting the adverse impact of uneven background in vessel segmentation process. Fig. 2.8 shows principal eigenvalue maps obtained for three retinal images with varying contrast. It can be observed that the background (non-vessel) pixels in the normalized eigenvalue maps have nearly identical pixel values, regardless of the contrast variation in original retinal images. This helps in segmentation of blood veins with a simple threshold technique.

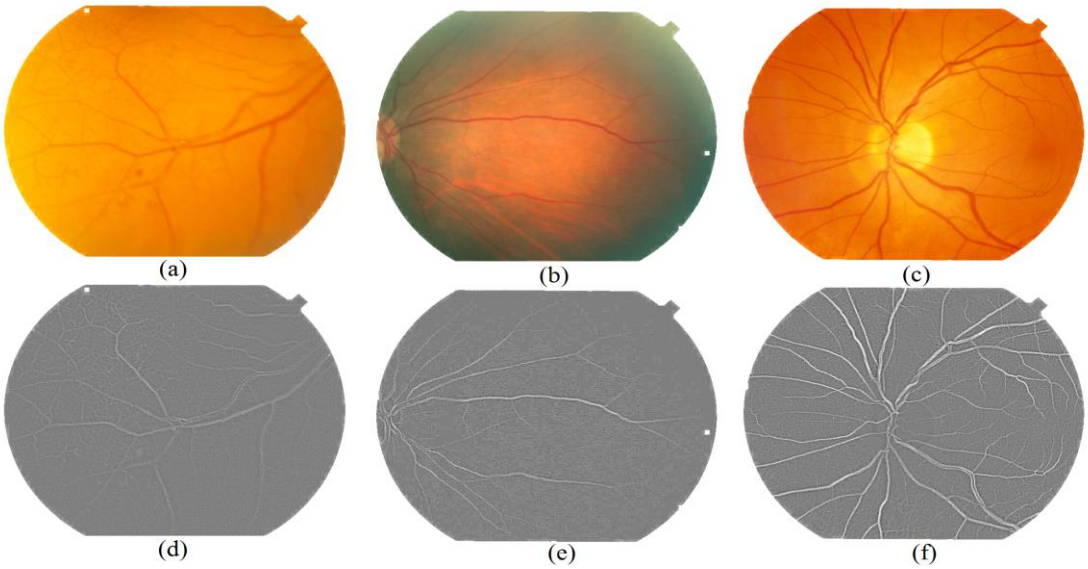

Fig. 2.8. Neutralizing the adverse effect of uneven background using local PCA: (a) low-contrast image; (b) image with varying contrast; (c) high contrast image; (d), (e) and (f) are the corresponding normalized principal eigenvalue maps.

In this work, the local PCA is performed at multiscale scales to enhance sensitivity of our methodology towards vessels with larger diameter. This is inspired by the multiscale analysis for vessel enhancement detailed in [2]. Specifically, we performed local PCA with two sets of kernels of dimentions 5×5 and 9×9. A normalization is then performed on the subsequent principal eigenvalue maps with the goal that they yield identical eigenvalues for areas of constant intensity. At last, normalized principal eigenvalue maps are combined by selecting the greatest eigenvalue (at each pixel area) among the maps at two investigation scales considered in this study.

2.2.2. Differential eigenvalue map

As depicted in Fig. 2.7, differential eigenvalue map comprises of differences between principal eigenvalue and the second eigenvalue as entries. Fig. 2.9 indicates differential eigenvalue of an example retinal image from DRIVE database. It may be noted that (refer to Fig.2.9 (b)) the differential guide clearly shows boundaries of veins. This is

because, the difference between the principal and the second eigenvalue becomes least at the vessel boundaries. We likewise have observed that locations of vessel boundary pixels got from differential eigenvalue map are consistent with that of edge pixels obtained by canny edge detector. In this work, the differential eigenvalue map is used to figure out a decision rule for connecting disconnected vessel segments, details of which are presented in the following section. For this purpose, a binary image is obtained by performing local thresholding of the differential eigenvalue map. Fig. 2.9(c) shows the resulting binary image. The thresholding operation is performed follows:

$$B_{x,y} = \begin{cases} 1, & \text{if } D_{\mathrm{x,y}} > mean \\ 0, & \text{otherwise.} \end{cases} \quad (15)$$

Where $B_{x,y}$ is the binary image obtained after performing thresholding operation on differential eigenvalue map $D_{\mathrm{x,y}}$ and $mean$ is the average of neighborhood pixels within the window of dimension 64×64.

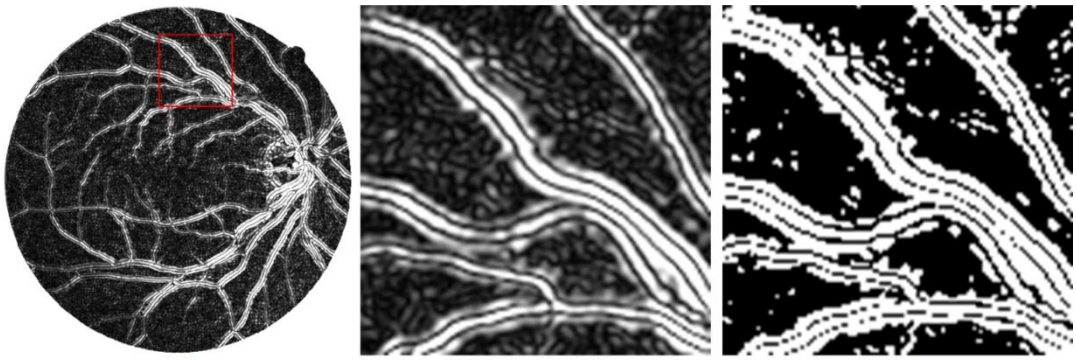

Fig. 2.9. Detecting boundaries of blood vessels: (a) Differential eigenvalue map; (b) A zoomed-in version of the selected region bounded by red colored rectangle in (a); (c) resulting binary image obtained by performing local thresholding on (b)

2.2.3. Selective growing of centerline pixels using differential eigenvalue map

Ideally, centerline pixels corresponding to the retinal vessel structure should be connected to each other. However, because of pathologies and extrudate in retinal images, some of the detected centerline pixels form small and isolated segments (Refer to Figs. 2.5(b) and 2.10(a)-(d)). Since these portions corresponds to true vessels are not connected to the main vessel structure, they may get filtered alongside isolated segments (relating to non-veins) while bounding rectangle constrained is imposed. Therefore, connection of all pixels belonging to vessel segments is crucial before

removal of small isolated segments that belongs to non-vessel structures. For this reason, a selective region growing is performed. In this methodology, pixels situated at the ends (pixels with a single neighbor) of segments are considered as initial seed points.

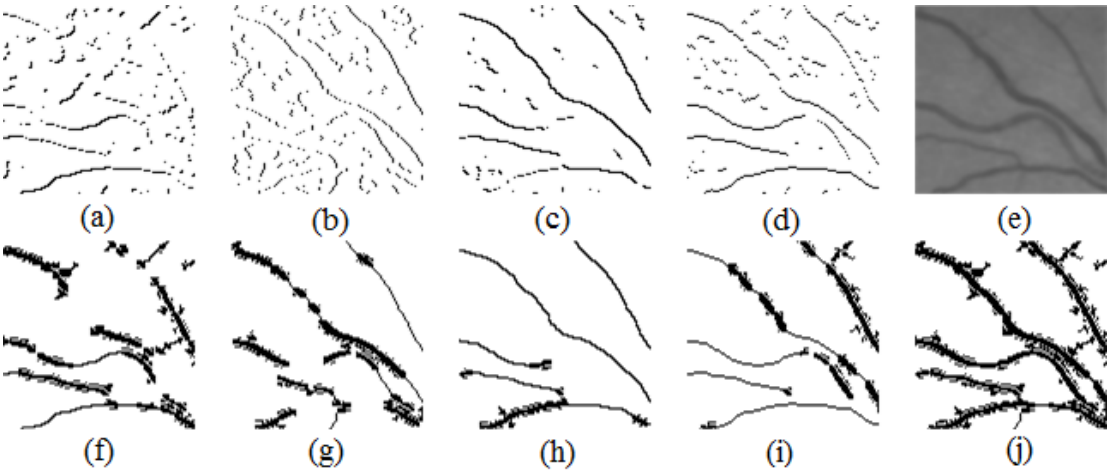

Fig. 2.10. Selective centerline pixel growing: (a), (b), (c) and (d) show centerline vessel pixels detected using -45 degree, horizontal, 45 degree, and vertical structuring elements respectively; (f), (g), (h), and (i) show corresponding images obtained by performing selective vessel growing and subsequently removing isolated segments; (e) and (j) show the original retinal image and the corresponding centerline image obtained by performing logical OR operation on images shown in (f), (g), (h), and (i).

Neighboring pixels are then added to the centerline vessel image, if pixel value at the corresponding location in the binary image (generated from the differential eigenvalue guide) is 1. In the proposed approach, the above procedure is iterated twice and is performed independently for each of the four centerline images generated utilizing different structuring elements. This is followed by filtering of isolated segments in each of the four centerline images utilizing bounding rectangle constraint. In particular, an 8-connected vessel segment is retained if its bouncing rectangle is totally contained in a square of dimension $W \times W$ pixels. In this study, we have emperically set the value of W to 30 and 50 for DRIVE and STARE databases, respectively. The above filtering operation is also performed independently for each of the four centerline images and the subsequent four images are consolidated using the logical OR operation. Intermediate results from the processing steps depicted in this section are shown in Fig. 2.10.

2.2.4. Retinal vessel extraction using principal eigenvalue map with refinement using centerline connectivity based decision rule

In this section, we present details of a methodology developed to segment blood vessels by removing background (non-vessel pixels), which generally has low principal eigenvalue when contrasted with regions containing blood vessels. Fig. 2.11 shows vessels extracted by thresholding principal eigenvalue map with a global threshold. The algorithm for determining this threshold is detailed in the following subsection. As can be seen in Fig. 2.11, a simple threshold based vessel extraction from principal eigenvalue map has high sensitivity.

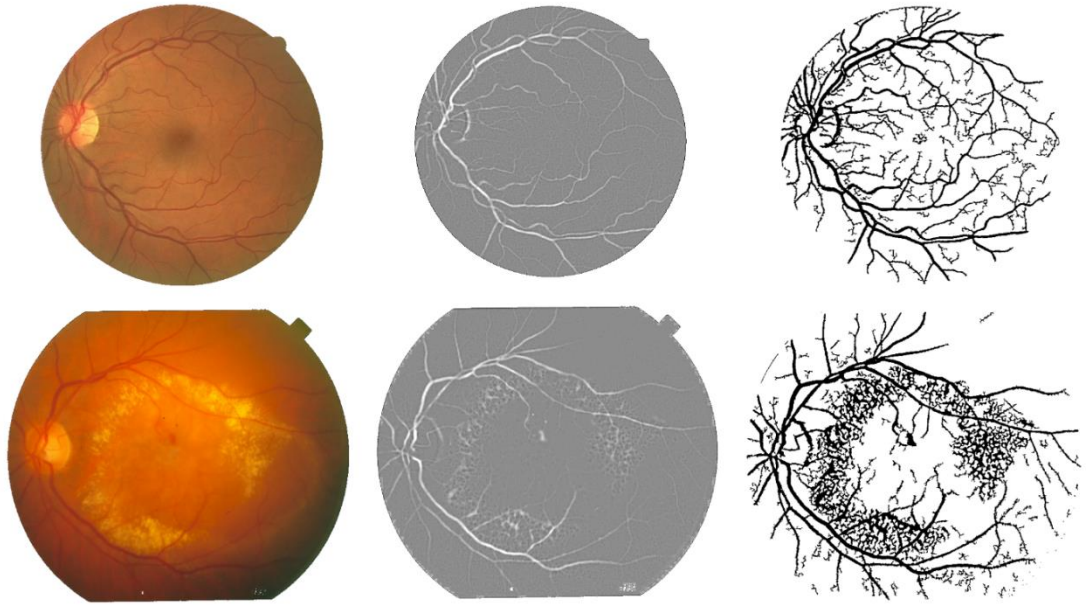

Fig. 2.11. Vessel extraction using principal eigenvalue map. The first column shows sample retinal images from DRIVE and STARE databases. The second and the third column show their corresponding principal eigenvalue maps and the extracted vessel structures.

However, it experiences poor specificity on account of pathologies and obscure vessel boundaries. To expel structures corresponding to pathologies from the segmented vessel image, a centerline based decision rule is applied to the segmented vessels. This operation is performed in two stages. In the first stage, thresholded principal eigenvalue map is ANDed with the centerline pixel image (obtained after performing vessel growing presented in Section 2.2.3) to expel structures corresponding to pathologies from the segmented vessel image. Other than removing pathological structures, the above operation serves another purpose. A portion of the connected structures of non-vessel pixels brought into the centerline image at the time of vessel growing get

separated forming small and isolated segments. Subsequently, a bounding rectangle constraint is forced on the ANDed image.

All vessel segments fulfilling bounding rectangle constraint are morphologically dilated and ANDed with vessel structure obtained from principal eigenvalue map in an attempt to restore to their original width. Intermediate results involved in the algorithm explained in this section are shown in Fig. 2.12. Section 2.3 describes a post-processing performed to refine boundaries of the identified vessels.

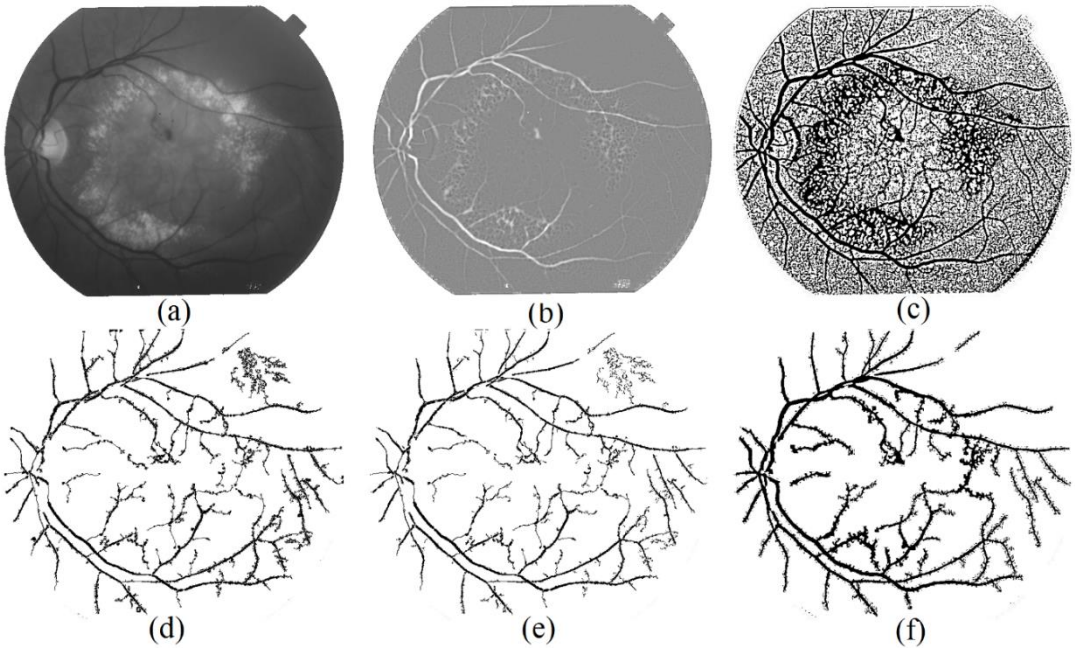

Fig. 2.12. Utilizing centerline information to remove pathological structures from vessel structure: (a) A retinal image with pathology (from the STARE database); (b) Principal eigenvalue map of the image shown in (a); (c) Thresholded principal eigenvalue map; (d) Centerline pixels; (e) Centerline pixels ANDed with image in (c); (f) Final vessel structure obtained using processing steps described in Section 2.2.3.

2.2.4.1 Deciding threshold for eigenvalue map

It has been observed that a vessel in low contrast region gets discarded when principal eigenvalue map is thresholded with a higher value (refer to Fig. 2.14(c)). On the other hand, a lower threshold results in noisy structures alongside true vessels as shown in Fig. 2.14(b). The normalized principal eigenvalue, computed using equations (1)-(6), for constant background of any intensity is 50. Therefore, the threshold value must be greater than 50. However, selecting a high threshold may lead to rejection of vessels in the low contrast region. Therefore, an empirically decided threshold of 50.25 is used for low contrast images, while a threshold of 50.5 is used for good contrast images. The flow diagram for computation of the threshold is shown in Fig. 2.13.

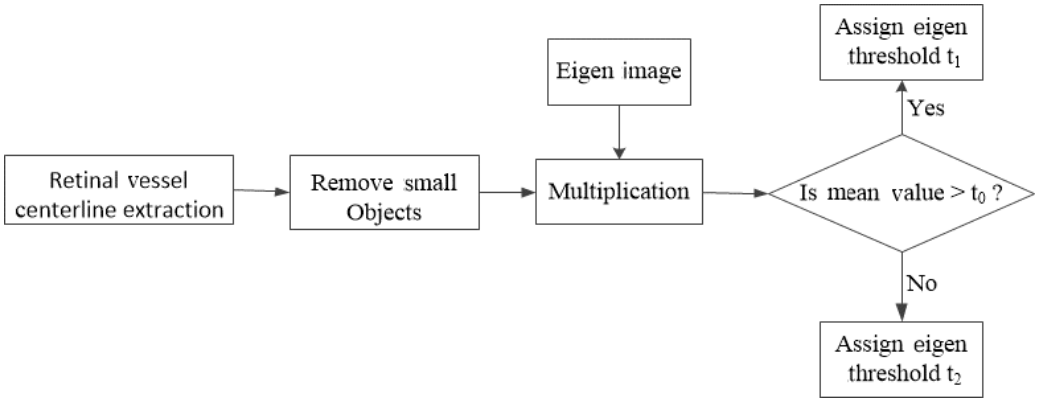

Fig. 2.13. Flow diagram to determine threshold for vessel detection from principal eigenvalue map.

An image is categorized as low contrast if the average of normalized principal eigenvalues calculated for centerline pixels is less than 51. Otherwise, the image is considered to be of good contrast.

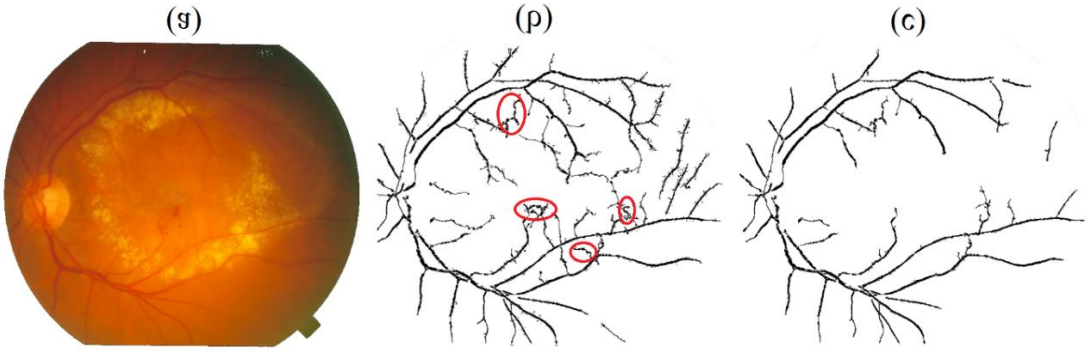

Fig. 2.14. Effect of threshold on the vessel structure obtained from principal eigenvalue map: (a) Noisy structures (shown in red circles) connected to the main vessel structure appear when a lower threshold (50.25) is selected; (b) True vessels, especially in the low contrast region are lost when a higher threshold (51) is selected.

2.3 Post-processing

The key objective of the post-processing stage is to minimize misclassified non-vessel pixels, particularly the ones that are appended to vessel boundaries. A closer look at the segmented vessel structures in Figs. 2.12(f) and 2.15(a) reveal many falsely detected structures. The misclassification emerges mostly because these non-vessel pixels are associated with the main vessel structure at boundaries and hence are not discarded by the bounding rectangle constraint.

The above observation motivated us to build up a post-processing method to eradicate erroneously recognized vessel pixels and thereby increasing the specificity of our approach. For this reason, we utilize vessel boundaries derived from differential eigenvalue map. As appeared in Fig. 2.9(b), these boundary pixels are portrayed by the

local minima in the differential eigenvalue map. Having identified vessel boundaries, pixels in the final segmented image (refer to Fig. 2.15(a)) that lie outside vessel boundaries are discarded. In particular this is accomplished by subtracting vessel boundary pixels from the final segmented

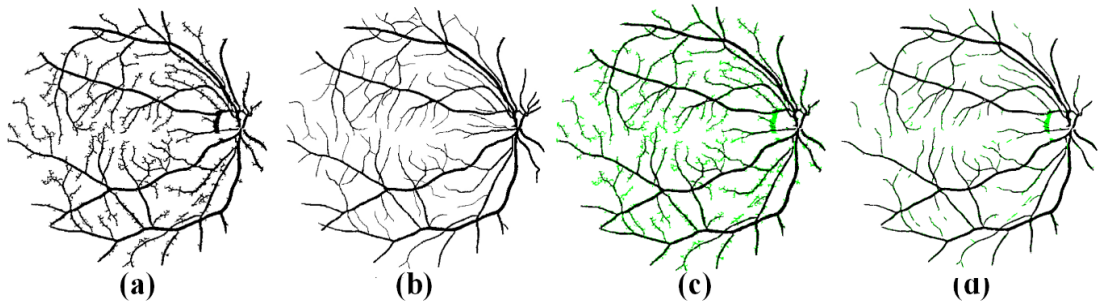

Fig. 2.15. Post-processing to improve specificity of vessel detection: (a) Blood vessel structure obtained using processing steps described in section 2.2.3; (b) Ground-truth; (c) Image in (a) with falsely detected vessel pixels in green color; (d) Vessel structure obtained after post-processing, showing significant reduction in number of falsely detected vessel pixels.

vessel image to isolate falsely detected vessels, which are shown by green colored pixels in Fig. 2.15(c). These isolated segments are then removed using previously discussed bounding rectangle constraint. However, in this process, boundary pixels are likewise lost. This effect is reversed by performing an iteration of morphological dilation and retaining only those pixels having corresponding principal eigenvalue of 50.5. This is performed based on our observation on vessel boundaries detected in poor contrast region (principal eigenvalue less than 50.5) having higher width than their true value.

2.4 Estimation of vessel width

In this section, we present an algorithm for estimation of retinal vessel width. The proposed algorithm makes use of principal and differential eigenvalue profiles to find two vessel boundary points on either side of a given center pixel. Algorithm 2 details the vessel width estimation approach and definition of notation adopted in this algorithm is presented in Table 2.1. Given the centerline pixel, the vessel width needs to estimated perpendicular to the local centerline direction, which can be estimated using two neighboring pixels on either side of the centerline pixel [53].

Principal and differential eigenvalue profiles are then extracted in this perpendicular direction. The neighborhood of the center pixel (in the principal eigenvalue profile) is analyzed to recognize the presence of central reflex and to

initialize the search for the boundary points. This is based on the observation that central reflex introduces a local minimum at (or close to) the centerline pixel in the principal eigenvalue profile, as shown in Fig. 2.16(a). On the other hand, profile of the principal eigenvalue map of a typical vessel without central reflex forms a concave region around the centerline pixel. Therefore, the nearby neighborhood of the centerline pixel in the principal eigenvalue profile are analysed to figure out whether the region is convex (indicating the presence of central reflex) or concave. A search for vessel boundary points is then performed primarily based on the principal eigenvalue with a threshold, which is set to 51 in our experiments. A differential eigenvalue based criterion is then used to refine the two identified boundary points, as demonstrated in the Algorithm 2.

In particular, when the value of principal eigenvalue is between 50.5 and 51, the vessel boundary points are incremented as long as they correspond to the falling edge of the differential eigenvalue profile. Fig. 2.16 shows principal and differential eigenvalue profiles comparing to two cases - a typical vessel and a vessel with central reflex.

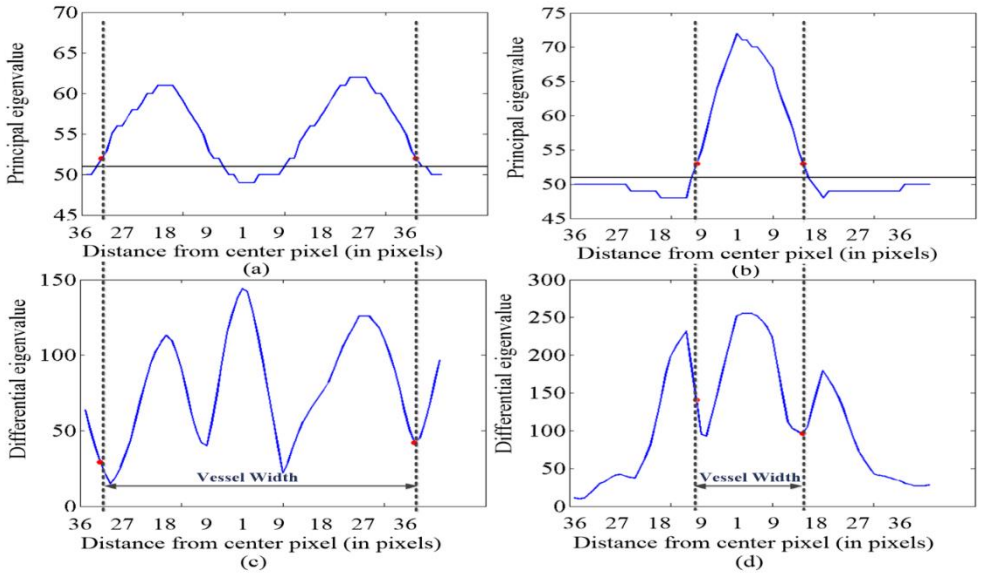

Fig. 2.16. Determining vessel boundary points using principal and differential eigenvalue profiles: (a) Principal eigenvalue profile of a blood vessel with central light reflex; (b) Principal eigenvalue profile of a blood vessel without central reflex; (c) and (d) are the corresponding differential eigenvalue profiles.

Table 2.1: Definition of notation

Notation	Definition
P	Principal eigenvalue profile at the center pixel and perpendicular to the vessel centerline (Refer to Fig. 2.16(a), (b))
D	Differential eigenvalue profile at the center pixel and perpendicular to the vessel centerline (Refer to Fig. 2.16(c), (d))
n	Pixel index and $\mathbf{n} \in [\boldsymbol{T_l}, \boldsymbol{T_r}]$
$\mathbf{pdist}(w_l, w_r)$	Function returns distance between points w_l and w_r
$\boldsymbol{w_l}$	Vessel boundary point on the left side of center pixel.
$\boldsymbol{w_r}$	Vessel boundary point on the right side of center pixel.
$\boldsymbol{t_l}, \boldsymbol{t_r}$	Variables $\boldsymbol{t_l} \in [1, \boldsymbol{T_l}]$ and $\boldsymbol{t_r} \in [1, \boldsymbol{T_r}]$
$\boldsymbol{T_l}, \boldsymbol{T_r}$	Variable $\boldsymbol{T_l} + \boldsymbol{T_r}$ determines the maximum vessel width that our algorithm can estimate

Algorithm 2: Vessel width estimation (**P, D**)

Input: P, D
Output: $\mathbf{pdist}(w_l, w_r)$
$w_l = 0, w_r = 0;$
if the neighborhood of center pixel is convex (valley)
  $t_l =$ nearest local maxima on left side
  $t_r =$ nearest local maxima on right side
    elseif the neighborhood of center pixel is concave (peak)
      $t_l = 1; t_r = 1;$
    end
end
for $n = t_l : 0.25 : T_l$
    if $\mathrm{P}(n) > 51$
      $w_l = w_l + 0.25;$
    end
    elseif $\mathrm{P}(n) >= 50.5$ and $\mathrm{D}(n) > D(n + 0.25)$
      $w_l = w_l + 0.25;$
    end
end
for $n = t_r : 0.25 : T_r$
    if $\mathrm{P}(n) > 51$
      $w_r = w_r + 0.25;$
  end
    elseif $\mathrm{P}(n) >= 50.5 \; and \; D(n) > D(n + 0.25)$
    $w_r = w_r + 0.25;$
  end
end
Return (pdist(w_l, w_r)**)**

Chapter 3

Proposed methodology for classification of epileptic seizure EEG signals

The block diagram of the proposed method for automated diagnosis of epilepsy using EEG signals is shown in Fig. 3.1.

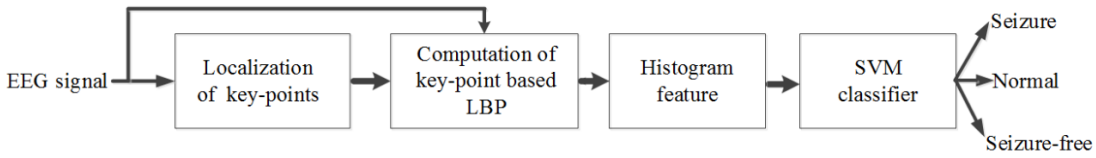

Fig. 3.1: Block diagram of the proposed methodology for classification of seizure, seizure-free, and normal EEG signals.

Details of the first stage in which the EEG signal is processed to identify a set of key-points are presented in the following section.

3.1. Detection of key-points in EEG signal

In order to detect key-points in EEG signals, we have adopted a technique employed in scale invariant feature transformation (SIFT) [54], which has been a very successful approach for image matching. Recently, a similar technique has also been investigated for gait based biometric recognition using data from accelerometer sensor [55]. The key-point detection technique employed in this work involves convolving the EEG signal with a set of Gaussian filters to smooth the signal progressively, which is achieved by incrementing the scale (standard deviation) of the Gaussian function. This process generates a set of Gaussian smoothed signals as illustrated in Fig. 3.2. A pyramid of difference of Gaussian (DoG) filtered signals are then generated by computing the differences of adjacent signals in the set of Gaussian smoothed signals. Maxima and minima (extrema) in each level of this pyramid forms the set of key-points. These key-points are identified by comparing a sample value in the DoG filtered signal with its two immediate neighbors and 3 neighbors each in the two adjacent (upper and

lower) levels in the pyramid. The detection of key-points is performed in each of the levels, except for two signals at the top and bottom of the DoG pyramid. The rest of this section provides a summary of the above discussed approach for detection of key-points in EEG signals through a set of mathematical equations.

The discrete-time Gaussian filter $g(n,\sigma)$ used in the key-point detection approach is obtained by sampling

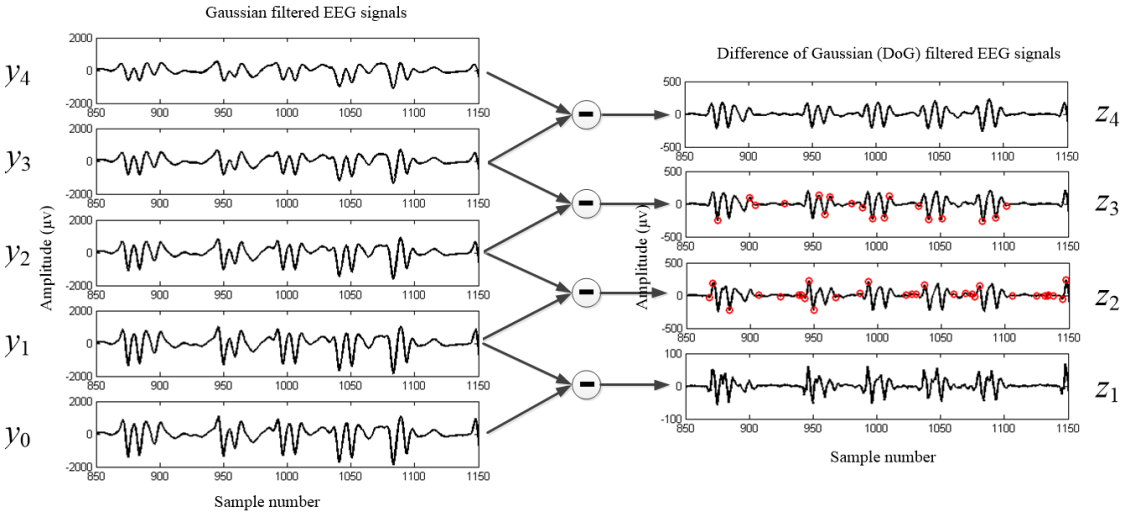

Fig. 3.2: Pyramid scheme for key-point localization with $M = 4$. Gaussian filtered signals are shown on the left side; the corresponding DoG filtered signals are shown on the right side and detected key-points are indicated by red circles.

the following continuous-time Gaussian function:

$$g(t,\sigma) = \frac{1}{\sqrt{2\pi\sigma^2}} e^{-t^2/2\sigma^2} \tag{1}$$

Where σ is the standard deviation of the Gaussian function. Convolution of the EEG signal $x(n)$ with a set of Gaussian filters can be represented as follows:

$$y_k(n) = x(n) * g(n, k\sigma_1) \qquad k = 1, 2, ..., M \tag{2}$$

where asterisk denotes the discrete convolution operation and σ_1 is the initial scale of the Gaussian filter. The set of signals in (2), along with the original EEG signal $x(n)$ (i.e., $y_0(n) = x(n)$) are then used to generate the pyramid of DoG filtered signals:

$$z_i(n) = y_{i-1}(n) - y_i(n) \qquad i = 1, 2, ..., M \tag{3}$$

Finally, key-points are detected in signals corresponding to each of the levels in the DoG pyramid. Locations of these key-points in terms of their sample indices and the level at which they are detected are taken forward for the next stage of processing. The

following section details the process of generation of the feature representation in the proposed method.

3.2. LBP based key-point descriptor

After detecting key-points in the EEG signal, the objective is to obtain a feature representation that carries sufficiently high discriminating ability for reliable classification of EEG signals. In this section, we present details of our feature extraction technique, which involves computing LBP [1] at every key-point detected in the signal. Specifically, LBPs are computed at the key-points detected in the DoG filtered signals ($z_i(n)$) as well as at the corresponding points in the original EEG signal ($x(n)$). In general, computation of LBP at a key- point located in a signal $f(n)$ can be mathematically expressed as follows:

$$\begin{aligned} LBP[f(i)] = &\sum_{j=0}^{3} S[f(i+j), f(i+4)]\,2^{j} + \\ &\sum_{j=5}^{8} S[f(i+j), f(i+4)]\,2^{j-1} \end{aligned} \tag{4}$$

where the function S, with $f(i)$ and $f(j)$ as input parameters is given by

$$S[f(i), f(j)] = \begin{cases} 1 & \text{for } f(i) \geq f(j) \\ 0 & \text{for } f(i) < f(j) \end{cases} \tag{5}$$

In equation (4), i denotes the sample index of the key-point at which the LBP is being computed. As can be seen in equation (4), the LBP is generated by considering a sample which lies four samples to the right of the key-point as the center sample. Four immediate neighbors on either side of this sample are thresholded against the center sample to generate an 8-bit binary code (refer to Fig. 3.3). The decimal equivalent of this code is the LBP. In this work, histogram of LBP is used as the feature set for classification of EEG signals. We have considered only uniform patterns in LBP [56], which contain at the most two transitions from 0 to 1 or 1 to 0. While the uniform patterns are mapped to their corresponding bins, all non-uniform patterns are mapped to a single bin. For our case (with 8-bit binary codes), this process generates a histogram feature of length 59.

It may be noted that each of the detected key-points has an associated level (or scale) in the DoG pyramid. Therefore, *LBP histograms (from DoG filtered as well as*

the original EEG signal) are computed separately for key-points corresponding to different levels.

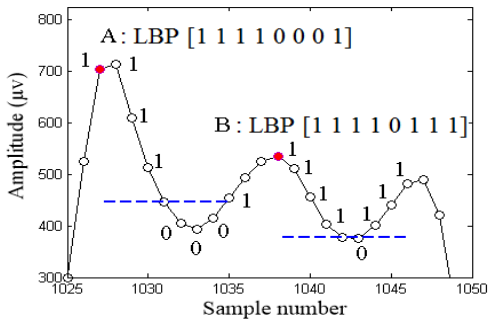

Fig. 3.3: Generation of LBP at two key-points in a segment of EEG signal is shown. The key-points are indicated by pink dots, while the corresponding threshold levels for neighborhood comparison are shown by blue dashed lines.

Since key-points cannot be detected in the top and bottom level of the DoG pyramid (due to the lack of signals at the upper or lower levels for these signals), this process generates as set of $M-2$ histograms from the DoG filtered EEG signals. Similarly, another set of $M-2$ LBP histograms are generated from the original EEG signal using LBPs computed at the points corresponding to the key-points. Finally, the two sets of LBP histograms are concatenated to obtain the final representation. For example, in this work, we have set value of the parameter M (number of levels in the pyramid) to 4. Therefore, we have LBP histograms computed at two levels. At each level, there is one histogram each from the DoG filtered signal as well as the original EEG signal. Since the length of each of the uniform LBP histograms is 59, their concatenation results in a feature vector of dimension 59 × 4.

The proposed feature extraction technique for EEG signal classification is motivated by an approach [56] developed for image matching using LBP for description of interest regions.

3.2.1. Classification

After computing the histogram of LBP as the feature for discrimination, the final task is to classify a given EEG signal into one of the three classes namely, seizure, seizure-free and normal. In this work, we have used the SVM classifier [57] for classification of EEG signals. More specifically, we have used the SVM classifier with radial basis function (RBF) kernel available in the WEKA machine learning toolbox [58]. In all our experiments, we have set the tradeoff parameter of the SVM and the kernel parameter sigma of the RBF kernel to 2.395 and 0.1, respectively.

Chapter 4

Performance evaluation and discussion

In this work two different methodologies, specifically a methodology for retinal blood vessel image segmentation and a methodology for classification of epileptic seizure EEG signals has been proposed for computer-aided diagnosis. The performance of these methodologies is evaluated on the benchmark databases and are detailed in the following sections.

4.1. Vessel segmentation

Performance of the proposed retinal vessel segmentation methodology is assessed on two freely available benchmark databases, namely DRIVE [10] and STARE [59]. In the literature, these databases have been widely used by researchers to assess vessel segmentation approaches. Aside from being openly available, manually segmented ground truth information is available for images in these databases. The DRIVE database consists of 40 retinal images and the entire set has been partitioned into a train and a test set with each set containing 20 colour retinal images. Two manually segmented vessel images are provided for each image in the test set, out of which the first one is considered the ground-truth (O_1) for the purpose of evaluation and the second one (O_2) is often reported as the human observer segmentation result for the purpose of comparison. The STARE database, collected by Hoover et al. [59], contains 20 fundus images (with ground-truths for vessels) captured with the field of view (FOV) of 35degree, and afterward digitized to obtain colour (RGB) retinal images. Ten of these images contain pathology, which pose major challenge in precise identification of vessel pixels. Manual labelling of the vessel structure for retinal images in the STARE database was performed by two different observers. Likewise with the DRIVE database, the first set of manually labeled vessel network is used as the ground-truth

segmentation result for computing the performance measures and the results are shown in Table 4.1. Moreover, we have performed another set of experiments with second observer's segmentation result as the ground-truth and the results are shown in Table 4.2. Performance of the proposed method was assessed using performance measures such as accuracy (ACC), sensitivity (SEN) and specificity (SPF). Performance of the proposed approach for vessel detection in terms of the above measures is shown (in boldface) in Table 4.1. As can be seen from this table, performance of our approach is better than majority of the existing unsupervised methods, with the exception of the three recently proposed ones [17, 25, 26]. Vessel detection accuracy of the proposed methodology is very much comparable with that of techniques presented in [17, 25, 26]. Specificity of our approach is likewise similar, and in some cases marginally better when contrasted with the above methods.

Table 4.1: Comparative performance of different segmentation methods in terms of accuracy, sensitivity and specificity on drive and stare datasets

Database / Method	STARE			DRIVE		
	ACC	**SPF**	**SEN**	**ACC**	**SPF**	**SEN**
2nd Human Observer (O_2)	0.935	0.9384	0.8951	0.947	0.972	0.776
Supervised Methods						
Ricci *et. al* [9]	0.965	0.939	0.903	0.959	0.972	0.775
Staal *et. al* [10]	0.952	0.981	0.697	0.944	0.977	0.719
Fraz *et. al* [11]	0.953	0.976	0.755	0.948	0.981	0.74
Soares *et. al* [12]	0.948	0.975	0.72	0.946	0.978	0.733
Marin *et. al* [13]	0.952	0.982	0.694	0.945	0.98	0.706
Niemeijer *et. al* [14]	-	-	-	0.942	0.969	0.689
Roychowdhury *et. al* [15]	0.951	0.973	0.772	0.952	0.983	0.725
Unsupervised Methods						
Mendonca *et. al* [16]	0.944	0.973	0.699	0.945	0.976	0.734
Zhao *et. al* [17]	0.956	0.978	0.780	0.954	0.982	0.742
Budai *et. al* [18]	0.938	0.982	0.58	0.957	0.987	0.644
Perez *et. al* [19]	0.926	0.944	0.769	0.925	0.967	0.644
Jiang *et. al* [20]	0.901	0.90	0.857	0.891	0.90	0.83
Lam and Yan [21]	0.947	-	-	-	-	-
Budai *et. al* [22]	0.938	0.975	0.651	0.949	0.968	0.759
Miri *et.al* [23]	-	-	-	0.943	0.976	0.715
Nguyen *et. al*[24]	0.932	-	-	0.941	-	-
Roychowdhury *et. al* [25]	0.956	0.984	0.732	0.949	0.978	0.739
Imani *et.al* [26]	0.9590	0.9745	0.7502	0.9523	0.975	0.754
Hoover *et. al* [59]	0.927	0.81	0.65	-	-	-
P.Bankhead *et. al* [60]	-	-	-	0.9371	0.972	0.703
Salazar-Gonzalez *et. al* [61]	0.9441	0.9633	0.7887	0.9412	0.968	0.752
Annunziata *et. al* [62]	0.9562	0.9836	0.7128	-	-	-
Proposed Method	**0.9552**	**0.9813**	**0.7283**	**0.9443**	**0.980**	**0.701**

However, sensitivity of our approach is lower than these methods on both of the databases. This is perhaps due to the post-processing stage involved in our approach.

Table 4.2: Performance measures from interobserver variability test on drive and stare datasets

Data	Ground-truth	ACC	SEN	SPF
DRIVE	O_1	0.9443	0.7014	0.9802
	O_2	0.9500	0.7327	0.9810
	$O_1 \cap O_2$	0.9584	0.8286	0.9727
STARE	O_1	0.9552	0.7283	0.9813
	O_2	0.9265	0.5679	0.9900
	$O_1 \cap O_2$	0.9592	0.7748	0.9781

A closer observation of our results (refer to Fig. 2.15) indicates false removal of vessels segments present in very low contrast regions and are not connected to main vessel structure. An examination with supervised techniques indicates that some of these techniques are plainly superior in performance, particularly the method proposed by Ricci et. al. [9] accomplished the highest sensitivity of about 90% and 77.5% on STARE and DRIVE databases, respectively. However, as discussed earlier, major drawback of supervised techniques (in general) is their reliance on the labeled training data. Ricci et. al. [9] showed the dependence of their classification method by training the classifier on either one of the DRIVE and STARE databases, and then, testing it on the other. They observed that the accuracy of their vessel classification technique disintegrated from 0.9595 to 0.9266 on DRIVE database when trained on STARE database. Similarly, the classification accuracy diminished from 0.9646 to 0.9452, when assessed on STARE database with training done on DRIVE images. Therefore, classifier retraining is necessary in some of the supervised algorithms. In addition to the classification performance, computational performance of the proposed methodology is extremely encouraging. On average, the proposed vessel segmentation approach requires 1.272 sec and 0.959 sec for segmenting a retinal image in the STARE and DRIVE databases, respectively. Our algorithm was implemented using LabVIEW on an Intel Core i5 PC, running at 3.1 GHz with 4-GB memory. Computational efficiency of our approach does away with the need for any high performance computing resources. In addition, it is a desirable feature for self-diagnostic applications in smartphones and other portable devices.

Additionally, we have evaluated our vessel segmentation method by considering second observer's segmentation (O_2) as the ground-truth. Performance measures from this set of experiments are shown in Table 4.2. Performance measures

with O_1 are also included in this table for comparison and to study the impact of observer variability on the performance of the proposed method. Fig. 4.1 shows inter-observer variability in segmentation results obtained by observer 1 and 2. In this figure, pixels with gray shade are the ones that are classified as vessel pixels in both O_1 and O_2, while the set of brighter pixels are the ones that are classified as vessel pixels in O_2 and as non-vessel pixels in O_1. From Fig. 4.1, it may be observed that the observer 2 consistently over-estimated vessel widths in STARE dataset as compared to O_1.

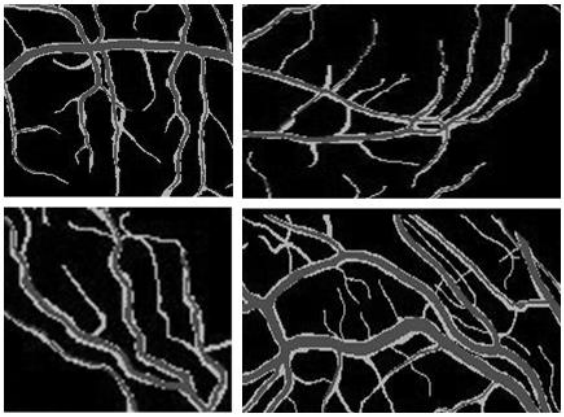

Fig. 4.1. Inter-observer variability in vessel segmentation results in STARE dataset

This perhaps clarifies why the sensitivity of our approach (in STARE dataset) decreased considerably when O_2 is considered as the ground-truth. We have carried out another analysis using a third ground-truth created by performing logical AND operation between ground-truths O_1 and O_2. The new ground-truth is expected to provide a better vessel width estimate as it contains those vessel pixels on which both observers agreed. Performance measures shown in Table 4.2 indicate that the accuracy and sensitivity our approach improved considerably with the new ground-truth, while there is marginal reduction in the performance in terms of specificity. In spite of the fact that the proposed methodology accomplishes relatively good retinal vessel segmentation results, some of the limitations of the method must be addressed by future work. As discussed earlier in this section, sensitivity of our approach can be improved by reducing false removal of vessels present in very low contrast region and are not linked to main vessel structure in the post-processing stage that means to enhance specificity. Moreover, false detection occurs in some of the images having pathologies, especially the ones which form elongated structures in the vessel centerline image. It is expected that the performance of a vessel segmentation methodology will degrade in regions of retinal images, where pathological structures such as red lesions, cotton-wool spots are present. Therefore, it is of interest to assess vessel segmentation methodology

separately on pathological images. In the literature, researchers have evaluated performance of their approaches on a subset [62] of STARE dataset that contains pathological structures.

Table 4.3: Comparative segmentation performance on the stare abnormal dataset

Method	ACC	Time
Soares *et. al* [12]	0.9425	3 mins
Marin *et. al* [13]	0.9510	90 s
Roychowdhury *et. al* [15]	0.9453	8.36 s
Mendonca *et. al* [16]	0.9426	3 mins
Jiang *et. al* [20]	0.9352	8-36 s
Lam and Yan [21]	0.9474	8 mins
Roychowdhury *et. al* [25]	0.9535	3.87 s
Hoover *et. al* [59]	0.9211	5 mins
Salazar-Gonzalez *et. al* [61]	0.9369	-
Annunziata *et. al* [62]	0.9565	25s
Lam *et. al* [63]	0.9556	13 mins
Vermeer *et. al* [64]	0.9287	-
Proposed Method	**0.9553**	**1.227 s**

We have also performed experiments on the same subset and the performance measure (computed using ground-truth O_1) obtained is reported in Table 4.3. It can be observed from the table that performance of the proposed approach is quite comparable to the ones in [61], [65] and outperforms rest of the techniques reported in the table. Another additional feature of our approach is its computational performance. The major difference between our approach and a previous study [27] that applied PCA for retinal vessel segmentation is that the proposed approach is based on eigenvalue decomposition of a matrix formed by second-order image moments. Eigenvalue decomposition in our approach yields a vessel enhanced image. On the other hand, the work reported in [27] is a supervised technique that employed ANN for classification of a pixel. The first component derived from PCA of retinal color image is used as a feature for ANN based classification. Another related work [2] is based on the eigenvalue decomposition of the Hessian matrix, which is formed by second-order derivatives of the image.

4.2. Vessel width measurement

Performance of the proposed vessel width measurement approach is evaluated using the REVIEW dataset [65], which comprises of four subsets namely, kick-point image set (KPIS), central light reflex (CLRIS), vascular disease (VDIS) and high-resolution

image set (HRIS). Details of the images in these subsets can be found in [65]. Altogether, the dataset consists of 16 high resolution images, ranging in size from 1360×1024 pixels to 3584×2438 pixels with 193 vessel segments marked by three observers. The mean of vessel widths defined by these observers is considered as the standard for evaluating vessel width measurement approach. The REVIEW dataset provides a pair of vessel edge points for each vessel profile, from which the center point and vessel width can be computed. Profile centre points from REVIEW dataset are used to initialize our vessel width measurement algorithm. Specifically, we have measured vessel widths at the nearest vessel centerline pixels corresponding to the profile center points in the REVIEW dataset. Performance measures for this set of experiments, namely, success rate (**%**), mean of vessel widths (**Mean)**, and standard deviation of measurement error **(σ_x)** have been adopted from previous works [28], [60].

Table 4.4: Comparative performance of vessel width measurement approaches on review dataset

Image-set / Method	KPIS			CLRIS			VDIS			HRIS		
	%	**Mean**	**σ_x**	**%**	**Mean**	**σ_x**	**%**	**Mean**	**σ_x**	**%**	**Mean**	**σ_x**
Standard	100	7.52	0.00	100	13.80	0.00	100	8.85	0.00	100	4.35	0.00
O_1	100	7.00	0.23	100	13.19	0.57	100	8.50	0.54	100	4.12	0.29
O_2	100	7.60	0.21	100	13.68	0.70	100	8.91	0.62	100	4.35	0.26
O_3	100	7.97	0.23	100	14.52	0.57	100	9.15	0.67	100	4.58	0.28
ESP [28]	100	6.56	0.33	93.0	15.7	1.47	99.6	8.80	0.77	99.7	4.63	0.42
IUWT [60]	100	6.30	0.29	100	14.27	0.95	99.0	8.07	0.95	99.5	4.66	0.32
Graph [66]	99.4	6.38	0.67	94.1	14.05	1.78	96.0	8.35	1.43	100	4.56	0.57
Gregson [67]	100	7.29	0.60	100	12.80	2.84	100	10.07	1.49	100	7.64	1.48
HHFW [68]	96.3	6.47	0.39	0	-	-	78.4	7.94	0.88	88.3	4.97	0.93
1DG [69]	100	4.95	0.40	98.6	6.30	4.14	99.9	5.78	2.11	99.6	3.81	0.90
2DG [70]	100	5.87	0.34	26.7	7.00	6.02	77.2	6.59	1.33	98.9	4.18	0.70
Proposed	**100**	**6.847**	**0.29**	**94.7**	**13.92**	**0.60**	**97.8**	**8.202**	**0.632**	**96.2**	**3.928**	**0.51**

Experimental results are presented in Table 4.4 together with performance measures of the existing methods for comparison. It can be observed that the performance of the proposed approach compares very favourably with [60] and [28].

4.3 Seizure classification

For evaluation of second methodology, we have used publically available dataset of EEG signals provided by University of Bonn, Germany [71]. This dataset contains EEG signals acquired from healthy subjects and patients (during and in the absence of seizure activity). The EEG recordings from healthy subjects are obtained in two conditions

namely, eyes open (EO) and eyes closed (EC), which are denoted by Z and O subsets in the dataset respectively. Each of these subsets (Z, O) has 100 surface recorded EEG signals. In the dataset, subsets N and F contain 100 EEG signals each recorded intracranially from the epileptic patients in the seizure-free intervals. The subsets N and F contain recording of EEG signals corresponding to epileptogenic zone and hippocampal formation, respectively. The subset S in the dataset contains 100 EEG signals acquired from epileptic patients during seizure activity. In this study, in order to evaluate the performance of the proposed method, we have considered four classification problems namely, normal (N) and epileptic seizure (ES); ES and seizure-free (SF); ES and non-seizure (NS); N, SF, and ES; we have formed the class N by combining subsets Z and O of the dataset. The ES class is obtained from the EEG signals of subset S. The subsets N and F grouped in order to obtain the SF class. The NS class contains EEG signals from the subsets Z, O, N, and F of the dataset. Therefore, we have considered the entire dataset for assessing performance of the proposed method. Sample EEG signals from N, SF, and ES are shown in Fig. 4.2.

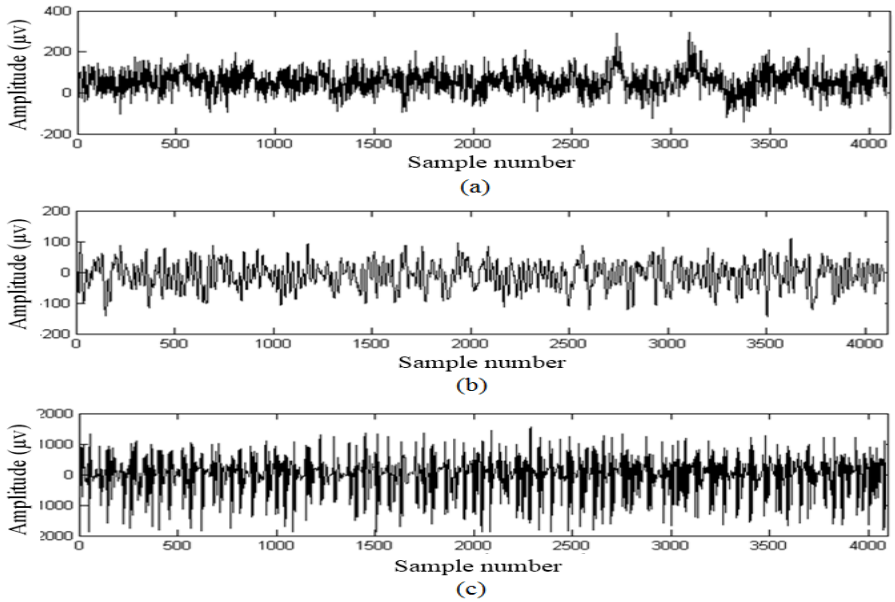

Fig. 4.2: Sample EEG signals from Bonn EEG dataset corresponding to normal (N), seizure-free (SF), and epileptic seizure (ES) are shown in (a), (b), and (c) respectively.

Brief descriptions of each of the classification problems, together with their significance are provided in the following part of this section:

(1) In the first classification problem, we have considered classification of normal EEG signals and epileptic seizure EEG signals. The automated method developed for

classification of epileptic seizure EEG signals from normal EEG signals can be used for identifying epileptic patients out of normal and epileptic patients.

(2) The second problem considered is classification of seizure-free and epileptic seizure EEG signals that can be used for detecting epileptic seizures in the epileptic patients.

(3) The third one is a more general classification problem which performs discrimination of normal, seizure and seizure-free EEG signals and can be used for automatic detection of epileptic seizures from non-seizure patients, which include normal and epileptic patients.

(4) The fourth classification problem that we have considered performs discrimination of normal, seizure and seizure-free EEG signals. The classification technique developed for this problem can be used for automated detection of epileptic patients during seizure activity or in the absence of seizure activity from the normal people. Details provided in this section are summarized in Table 4.5.

Table 4.5: Composition of classes considered for the four classification problems.

Classification problem	Classes	Number of EEG signals
1	Normal (Z,O) Seizure (S)	200 100
2	Seizure-free (N,F) Seizure (S)	200 100
3	Non-seizure (Z,O,N,F) Seizure (S)	400 100
4	Normal (Z,O) Seizure-free (N,F) Seizure (S)	200 200 100

In addition to the University of Bonn EEG dataset, we have accessed the EEG dataset collected at Sir Ganga Ram Hospital in New Delhi [72]. This dataset consists of digitized (with a sampling frequency of 400 Hz) EEG recordings of a number of epileptic patients. Acquisition of these EEG signals involved placing 16 electrodes on the subject's scalp according to the international 10–20 system. The dataset is divided (with the help of neurologists) into two subsets, with the first subset containing EEG signals captured during seizure activity and the second one containing seizure-free EEG signals of the same set of patients. Each of these subsets contains 100 EEG signal segments, each of 3 seconds duration. This dataset has been used for evaluating performance of the proposed method for the second (seizure-free and seizure) classification problem.

4.3.1 Results

The proposed method has been evaluated using 10-fold cross-validation and commonly used performance measures such as accuracy (ACC), sensitivity (SEN), specificity (SPE), positive predictive value (PPV), negative predictive value (NPV) and Matthews correlation coefficient (MCC) [73]. It may be noted that larger the MCC value, the better will be the classifier performance. In the proposed method, there are two parameters namely, number of levels (M) in the DoG pyramid and the initial scale (σ_1) of the Gaussian filter. In all our experiments, we have set the value of σ_1 to 0.5. Since the scale parameters of successive Gaussian filters are related to the initial one through (2), the 3-dB cutoff frequencies of the four Gaussian filters are 61.9 Hz, 25.5 Hz, 18.5 Hz and 13 Hz. To study the influence of the parameter M on the classification performance, we have carried out a set of experiments by varying its value. As described in section 3.1, the detection of key-points is performed through comparison of sample values of signals in the immediate upper and lower levels in the DoG pyramid. Therefore, key-point detection cannot be performed on the signals at the top and bottom of the DoG pyramid. This limits the minimum value of the parameter M to 3. Therefore, we have varied the value of this parameter, starting with the value of 3. Table 4.6 shows the performance measures achieved for four classification problems considered in this study. As can be seen in this table, our approach achieves high classification accuracies even with the minimum value of the parameter M. Incrementing the value of this parameter to 4 further improved the classification accuracies for all problems. Therefore, we have fixed the value of this parameter to 4 for further analysis.

With the above mentioned experimental setting, the classification accuracy of the proposed approach, together with performance of the existing techniques for each of the four problems is presented in Tables 4.7-4.10. To obtain better estimates of the performance, we have repeated 10-fold cross-validations 25 times. Therefore in Tables 4.7-4.10, we report mean and standard deviation (the number within the parenthesis) of the classification accuracy. It may be noted that the proposed method provides high classification accuracy consistently for the four classification problems.

Table 4.6: Performance measures from our experiments which are carried out by varying the number of levels in the DoG pyramid

Pyramid level	Classification task	ACC	SEN	SPE	PPV	NPV	MCC
4	ZO-S	100.0	100.0	100.0	100.0	100.0	1.00
	NF-S	99.45	99.68	99.00	99.52	99.42	0.99
	ZONF-S	99.31	99.68	97.85	99.48	98.79	0.98
	ZO-NF-S	98.80	-	-	-	-	-
3	ZO-S	100.0	100.0	100.0	100.0	100.0	1.00
	NF-S	99.27	99.40	99.00	99.52	98.91	0.98
	ZONF-S	99.10	99.30	98.60	99.33	98.76	0.98
	ZO-NF-S	98.20	-	-	-	-	-

Table 4.7: Performance comparison with the previous works for classification of normal and epileptic seizure EEG signals.

Method	Classification task	Accuracy (%)
Kaya *et al.* (2014) [1]	Z-S	99.50
Subasi and Gursoy (2010) [38]	Z-S	99.50
Pachori et al. (2015) [45]	Z-S	100.0
Srinivasan *et al.* (2007) [49]	Z-S	100.0
Peker *et al*. 2015[74]	Z-S	100.0
Fu. *et al.* (2014) [75]	Z-S	99.13
Samiee *et al*. 2015[76]	Z-S	99.80
Parvez *et al*. 2015 [77]	Z-S	100.0
Guo *et al*. (2010) [78]	Z-S	99.60
Chen *et al*. 2014[79]	ZO-S	100.0
Guo *et al.* (2010) [79]	Z-S	99.85
Guo *et al.* (2011) [80]	Z-S	99.20
Iscan *et al.* (2011) [81]	Z-S	100.0
Lima *et al.* (2010) [82]	Z-S	100.0
Orhan *et al.* (2011) [83]	Z-S	100.0
Tzallas *et al.* (2007) [84]	Z-S	100.0
Übeyli (2010) [85]	Z-S	100.0
Wang *et al.* (2011) [86]	Z-S	100.0
Proposed method	**ZO-S**	**100.0 (0.00)**

Table 4.8: Performance comparison with the previous works for classification of non-seizure and epileptic seizure EEG signals.

Method	Classification task	Accuracy (%)
Bajaj and Pachori (2012) [42]	ZONF-S	99.50-100.0
Peker *et al*. (2015)[74]	ZONF-S	99.15
Samiee *et al*. (2015)[76]	ZONF-S	98.10
Chen *et al*. (2014)[78]	ZONF-S	100.0
Guo *et al*. (2010) [79]	ZONF-S	98.27
Orhan *et al.* (2011) [83]	ZONF-S	99.60
Tzallas *et al*. (2007) [84]	ZONF-S	97.73
Guo *et al.* (2010) [92]	ZONF-S	97.77
Ocak (2009) [93]	ZONF-S	96.65
Proposed method	**ZONF-S**	**99.31 (0.17)**

Table 4.9: Performance comparison with the previous works for classification of seizure-free and epileptic seizure EEG signals.

Method	Classification task	Accuracy (%)
Kaya *et al*. (2014) [1]	NF-S	97.00
Joshi *et al.* (2014) [33]	NF-S	95.33
Kumar *et al*. (2015)[35]	NF-S	98.33
Pachori and Patidar (2014) [41]	NF-S	95.75
Samiee *et al*. (2015)[76]	F-S	94.90
Proposed method	**NF-S**	**99.45 (0.25)**

Table 4.10: Performance comparison with the previous works for classification of normal, seizure-free, and epileptic seizure EEG signals.

Method	Classification task	Accuracy (%)
Kaya *et al*. (2014)[1]	Z-F-S	95.67
Ghosh-Dastidar *et. al*. (2008) [34]	Z-F-S	96.6
Acharya *et al.* (2011) [46]	Z-F-S	95.60
Acharya *et al.* (2009)[47]	ZO-NF-S	95.00
Acharya *et al.* (2011) [48]	Z-F-S	98.50
Peker *et. al*. (2015)[74]	Z-F-S	99.30
Peker *et. al*. (2015) [74]	ZO-NF-S	98.28
Guo *et al.* (2011) [80]	Z-F-S	93.50
Orhan *et al*. (2011) [83]	ZO-NF-S	95.60
Orhan *et al*. (2011) [83]	Z-F-S	96.67
Tzallas *et al*. (2007) [84]	ZO-NF-S	97.72
Tzallas *et al.* (2007) [84]	Z-F-S	99.28
Acharya *et al.* (2012) [87]	Z-F-S	99.70
Acharya *et al.* (2012) [88]	ZO-NF-S	98.10
Acharya *et al*. (2012) [89]	Z-F-S	99.00
Chua *et al.*(2011) [90]	Z-F-S	93.11
Faust *et al.* (2010) [91]	Z-F-S	93.30
Proposed method	**ZO-NF-S**	**98.80 (0.11)**

To further ascertain the effectiveness of the proposed methodology, we have evaluated its performance for classification of seizure and seizure-free EEG signals on the second dataset. The proposed method yielded classification performance of 99.89 (0.23), 100.0 (0.00) and 99.78 (0.46) for ACC, SEN and SPE, respectively. These experimental results further demonstrate that the proposed key-point based LBP approach is effective for discriminating seizure and seizure-free EEG signals with high accuracy.

We have also performed additional experiments to study the effect of length of EEG signal on the classification performance and to compare performance of our method with the existing LBP based method. Details of these experiments and results thereof are presented in the following sections.

4.3.1.1 Effect of length of EEG signal on the classification performance

In this section, we present results from our experiments that have been performed to study the effect of length **(N)** (or duration) of recorded EEG signal on the classification performance. This study is important as it helps us identify the minimum length of the

Table 4.11: Performance measures from our experiments which are carried out to study the effect of length of the recorded EEG signal on the classification performance.

Length N	Classification task	ACC	SEN	SPE	PPV	NPV	MCC
	ZO-S	100.0 (0.00)	100.0 (0.00)	100.0 (0.00)	100.0 (0.00)	100.0 (0.00)	1.00 (0.00)
	NF-S	99.45 (0.25)	99.68 (0.37)	99.00 (0.00)	99.52 (0.00)	99.42 (0.66)	0.99 (0.01)
	ZONF-S	99.31 (0.17)	99.68 (0.12)	97.85 (0.49)	99.48 (0.12)	98.79 (0.44)	0.98 (0.01)
4000	ZO-NF-S	98.80 (0.11)	-	-	-	-	-
	ZO-S	99.97 (0.09)	100.0 (0.00)	99.92 (0.28)	99.96 (0.13)	100.0 (0.00)	0.99 (0.00)
	NF-S	97.79 (0.23)	98.66 (0.35)	96.04 (0.20)	98.11 (0.11)	97.52 (0.62)	0.95 (0.01)
	ZONF-S	98.18 (0.23)	99.35 (0.20)	93.52 (0.77)	98.43 (0.18)	97.53 (0.73)	0.94 (0.01)
1000	ZO-NF-S	96.71 (0.23)	-	-	-	-	-
	ZO-S	98.63 (0.29)	99.94 (0.17)	95.34 (0.99)	98.26 (0.36)	99.84 (0.45)	0.97 (0.01)
	NF-S	96.90 (0.38)	99.67 (0.64)	93.84 (0.68)	95.15 (0.60)	99.66 (0.68)	0.94 (0.01)
	ZONF-S	98.86 (0.26)	99.99 (0.07)	94.77 (1.12)	98.62 (0.30)	99.95 (0.22)	0.97 (0.01)
250	ZO-NF-S	94.20 (0.17)	-	-	-	-	-
	ZO-S	92.47 (0.51)	94.50 (0.50)	88.40 (0.89)	94.41 (0.46)	89.67 (0.95)	0.83 (0.01)
	NF-S	94.80 (0.51)	97.50 (0.50)	89.40 (0.89)	95.05 (0.46)	95.07 (1.10)	0.88 (0.01)
	ZONF-S	94.12 (0.18)	96.30 (0.11)	85.40 (0.89)	96.46 (0.19)	86.87 (1.03)	0.82 (0.01)
50	ZO-NF-S	87.90 (0.17)	-	-	-	-	-

EEG signal that can provide satisfactory performance for classification problems considered in this study. For this purpose, we have performed a set of experiments by successively reducing the length of the EEG segment (N). Effectively, we have considered only first N samples of the original EEG signal for each of these experiments [40]. Results from our experiments are summarized in Table 4.11, which indicate that our approach achieves nearly perfect classification even with a segment length of 1000 samples for classification of normal and seizure EEG signals. More importantly, it can be observed that significant reduction in the segment length causes only marginal deterioration in classification performance. Specifically, a reduction in EEG signal length by a factor of 4 deteriorates the classification accuracy for the three-class (ZO-NF-S) classification problem by only about 2%. Results presented here indicate that our approach is well suited for online detection problems as well.

An additional experiment has been performed, in which we have randomly generated the sample number (index) of the initial sample. This initial sample and the N-1 succeeding samples are then extracted to obtain an EEG segment of length N, as opposed to first N samples considered in the previous experiment. However, as in the previous case, we have extracted only one segment from each EEG signal to ensure that the number of segments remains the same as in the original dataset. For a segment length of 1000 samples, the proposed method yielded classification accuracies of 99.54 (0.3), 96.23 (0.61), 98.04 (0.40) and 95.68 (0.34) for ZO-S, NF-S, ZONF-S and ZO-NF-S classification problems, respectively. This indicates a marginal deterioration in performance when segments are extracted randomly. From the experimental results presented in this section, it may be noted that the way in which EEG segments are extracted has very little influence on the performance of the proposed method. Therefore, the proposed method is robust to the selection of segments of EEG signals for the automated diagnosis of epilepsy.

4.3.1.2 Performance comparison with the existing LBP based method

To further ascertain the performance of our approach, we have performed a comparative evaluation with the conventional LBP based technique [1]. Specifically, we have evaluated performance of our approach on the datasets considered for classification in [1]. Results from this set of experiments are presented in Fig. 4.3. As can be seen in this figure, the proposed key-point based LBP approach yields consistently better classification accuracy for all the dataset combinations considered for classification in [1]. Since the method reported in [1] computes LBP at every sample in the EEG signal, it is highly likely that there are more number of noise features (which are not useful and may have an adverse effect on the classification accuracy) in the feature set as compared to the proposed method, which computes LBP only at the detected key-points. This perhaps explains why our method performs significantly better.

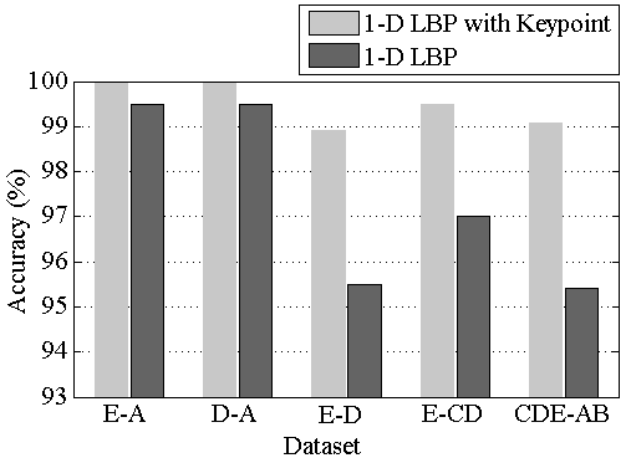

Fig. 4.3: Performance comparison with the existing LBP based method

Experimental results presented in this section indicate that the proposed method can be employed for effective EEG based computer-aided diagnoses of epilepsy. The performance of the proposed method is quite encouraging even when only 1000 samples of the EEG signal is used for classification. Moreover, the LBP descriptor employed in our method is known to be computationally simple. The above features of our method make it potentially useful for real-time seizure detection in devices with low computational and memory resources.

On the other hand, the size of EEG datasets used in this study for performance evaluation is limited. Therefore, our approach should be evaluated on larger databases before its clinical deployment. This aspect would be of interest in our future work. Another drawback of our method is that its computational complexity is slightly higher than that of conventional LBP based approach [1]. This is primarily due to the additional processing, which is required for localization of key-points in our approach.

Chapter 5

Conclusion and future work

In this work, two different methodologies has been presented that can be used in implementation of effective CAD system, specifically an approach for retinal vessel segmentation and an approach for seizure classification is detailed. The proposed approach for vessel segmentation utilizes eigenvalues of local covariance matrices, which are formed using second order image moments computed in the local neighborhood of every pixel. The vessel structure obtained by thresholding the principal eigenvalue map is refined using a set of vessel centerline pixels, along with vessel boundary information derived from differential eigenvalue map. In this work, vessel centerline pixels are detected using a simple yet efficient algorithm that employs a set of directional structuring elements. The proposed approach for centerline vessel detection has inherent sensitivity for slender vessels and vessels in the low contrast region. In the final stage, post-processing of the vessel structure is performed with a goal to enhance specificity of the vessel detection approach. Besides, we have developed an algorithm for measurement of vessel width using principal and differential eigenvalue profiles.

The performances of the proposed vessel segmentation and width measurement approaches have been observed to be quite comparable with the state-of-the-art in this area. Another advantage of the proposed vessel segmentation approach is its computational performance, which makes it suitable for real-time applications in portable devices. An intermediate result in the proposed method is the principal eigenvalue map, which could possibly be thresholded using a probing technique presented in [59] to yield a better estimate of the vessel structure. It would also be interesting to integrate our approach with the one presented in [17], by considering principal eigenvalue map explored in this work as vessel enhanced image in [17]. We also plan to investigate utility of our vessel detection approach for other applications

including palm-vein detection in near-infrared (NIR) images for biometric recognition tasks.

Moreover, we have also proposed a key-point LBP based novel methodology for automated diagnosis of epilepsy from EEG signals. The methodology has been studied for four well-studied classification problems namely, normal and epileptic seizure; epileptic seizure and seizure-free; epileptic seizure and non-seizure; normal, epileptic seizure, and seizure-free classes of EEG signals on two datasets. The performance of the proposed method has been compared with the existing methods for classification of these four classification problems in terms of classification accuracy on the University of Bonn EEG dataset. The proposed method has provided consistent improvement in classification accuracy over the conventional LBP based method. The clinical significance of the proposed method arises from its key features, which include high classification accuracy and computational simplicity of LBP features. More importantly, the proposed methodology has provided sufficiently high classification accuracy, even with considerably smaller segment of the EEG signal, thereby making it suitable for online epileptic detection with reduced computational burden. In future, we plan to investigate applicability of the proposed methodology for classification of other biomedical signals such as electrocardiogram (ECG), electromyogram (EMG) corresponding to normal and abnormal states. In addition, we also intend to improve the computational performance of our method by simplifying the process of detection of key-points.

REFERENCES

[1] Kaya, M. Uyar, R. Tekin and S. Yldrm "1D-local binary pattern based feature extraction for classification of epileptic EEG signals", *Appl. Math. Comput*., pp.209 -219, 2014

[2] R. F. Frangi, W. J. Niessen, K. L. Vincken, and M. A. Viergever, "Multiscale vessel enhancement filtering," *in Medical Image Computing and Computer-Assisted Interventation—MICCAI'98*. NewYork: Springer, 1998, vol. 1496, LNCS, pp. 130–137.

[3] H. R. Taylor and J. E. Keeffe, "World blindness: A 21st century perspective," *Brit. J. Ophthalmol*., vol. 85, pp. 261–266, 2001.

[4] S. Wild, G. Roglic, A. Green, R. Sicree, and H. King, "Global prevalence of diabetes: Estimates for the year 2000 and projections for 2030," *Diabetes Care*, vol. 27, pp. 1047–1053, 2004.

[5] T.T. Nguyen,J.J. Wang, and T.Y. Wong, "Retinal vascular changes in pre-diabetes and prehypertension," New findings and their research and clinical implications. *Diabetes Care*, vol. 30, pp. 2708–2715, 2007.

[6] M. Ortega, C. Marino, M. G. Penedo, and M. Blanco, F. Gonzalez, "Biometric authentication using digital retinal images," *in Proceedings of the 5th WSEAS International Conference on Applied Computer Science* , pp. 422-427, Apr. 2006.

[7] C. Mariño, M. G. Penedo, M. Penas, M. J. Carreira, and F. González, "Personal authentication using digital retinal images," *J. Pattern Anal.Appl*., vol. 9, no. 1, pp. 21–33, 2006.

[8] Z. Han, Y. Yin, X. Meng, G. Yang, and X. Yan, "Blood vessel segmentation in pathological retinal image," *Data Mining Workshop* ,pp. 960-967, 2014.

[9] E. Ricci and R. Perfetti, "Retinal blood vessel segmentation using line operators and support vector classification," *IEEE Trans. Med. Imag*., vol. 26, no. 10, pp. 1357–1365, Oct. 2007.

[10] J. Staal, M. Abramoff, M. Niemeijer, M. Viergever, and B. van Ginneken, "Ridge-based vessel segmentation in color images of the retina," *IEEE Trans. Med. Imag*., vol. 23, no. 4, pp. 501–509, Apr. 2004.

[11] M. M. Fraz, P. Remagnino, A. Hoppe, B. Uyyanonvara, A. R. Rudnicka, C. G. Owen and S. A. Barman, "An ensemble classification-based approach applied to retinal blood vessel segmentation," *IEEE Trans. Biomed. Eng*., vol. 59, no. 9, pp. 2538–2548, Jun. 2012.

[12] J. V. B. Soares, J. J. G. Leandro, R. M. Cesar Jr., H. F. Jelinek and M. J. Cree, "Retinal vessel segmentation using the 2-D Gabor wavelet and supervised classification," *IEEE Trans. Med. Imag*., vol. 25, no. 9, pp. 1214–1222, Sep. 2006.

[13] D. Marin, A. Aquino, M. Gegundez-Arias, and J. Bravo, "A new supervised method for blood vessel segmentation in retinal images by using gray-level and moment invariants-based features," *IEEE Trans. Med. Imag*., vol. 30, no. 1, pp. 146–158, Jan. 2011.

[14] M. Niemeijer, J. J. Staal, B. van Ginneken, M. Loog and M. D. Abrmoff, "Comparative study of retinal vessel segmentation methods on a new publicly available database," *Proc. Med. Imag. SPIE*, vol. 5370, pp. 648–656, 2004.

[15] S. Roychowdhury, D. Koozekanani, K. Parhi, "Blood vessel segmentation of fundus images by major vessel extraction and sub-image classification," *IEEE J. Biomed. Health Informat*., vol. 19, no. 3, pp. 1118–1128, May 2015.

[16] A. Mendonca and A. Campilho, "Segmentation of retinal blood vessels by combining the detection of centerlines and morphological reconstruction*," IEEE Trans. Med. Imag.*, vol. 25, no. 9, pp. 1200–1213, Aug. 2006.

[17] Y. Zhao, L. Rada, K. Chen, S. Harding, and Y. Zheng, "Automated vessel segmentation using infinite perimeter active contour model with hybrid region information with application to retina images," *IEEE Trans. Med. Imag*., vol. 34, no. 9, pp. 1797–1807, Aug. 2015.

[18] A. Budai, R. Bock, A. Maier, J. Hornegger, and G. Michelson, "Robust vessel segmentation in fundus images," *Int. J. Biomed. Imag*., article 154860, 2013.

[19] M. Palomera-Pérez, M. Martinez-Perez, H. Benítez-Pérez, and J. Ortega-Arjona, "Parallel multiscale feature extraction and region growing: Application in retinal blood vessel detection," *IEEE Trans.Inf. Technol. Biomed*., vol. 14, pp. 500–506, Mar. 2010.

[20] X. Jiang and D. Mojon, "Adaptive local thresholding by verification based multithreshold probing with application to vessel detection in retinal images," *IEEE Trans. Pattern Anal. Mach. Intell*., vol. 25, no. 1, pp. 131–137, Jan. 2003.

[21] B. Lam and H. Yan, "A novel vessel segmentation algorithm for pathological retina images based on the divergence of vector fields," *IEEE Trans. Med. Imag*., vol. 27, no. 2, pp. 237–246, Feb. 2008.

[22] A. Budai, G. Michelson, and J. Hornegger, "Multiscale blood vessel segmentation in retinal fundus images," *Proc. Bildverarbeitung fur die Med*.,pp. 261–265, Mar. 2010.

[23] M. Miri and A. Mahloojifar, "Retinal image analysis using curvelet transform and multistructure elements morphology by reconstruction," *IEEE Trans. Biomed. Eng*., vol. 58, no. 5, pp. 1183–1192, May 2011.

[24] U. T. V. Nguyen, A. Bhuiyan, L. A. F. Park and K. Ramamohanarao, "An effective retinal blood vessel segmentation method using multi-scale line detection," *Pattern Recogn*., vol. 46, no. 3, pp. 703–715, Mar. 2013.

[25] S. Roychowdhury, D. Koozekanani, and K. Parhi, "Iterative vessel segmentation of fundus images," *IEEE Trans. Biomed. Eng*., vol. 62, no. 7, pp. 1738–1749, June 2015.

[26] E. Imani, M. Javidi, and H.R. Pourreza, "Improvement of retinal blood vessel detection using morphological component analysis," *Comput. Methods Programs Biomed*., vol. 118, no. 3, pp. 263-279, Mar. 2015.

[27] M. M. Fraz, P. Remagnino, A. Hoppe, B. Uyyanonvara, A. R. Rudnicka, C. G. Owen, and S. A. Barman, "Blood vessel segmentation methodologies in retinal images–A survey," *Comput. Methods Programs Biomed*., vol. 108, pp. 407–433, 2012.

[28] B. Al-Diri, A. Hunter and D. Steel, "An active contour model for segmenting and measuring retinal vessels," *IEEE Trans. Med. Imag*., vol. 28, no. 9, pp. 1488–1497, Sep. 2009.

[29] Peek Vision, 'Professional eye exams from a phone', 2015. [Online]. Available: http://www.peekvision.org/. [Accessed: 10-Sep- 2015].
[30] U.R. Acharya , S.V. Sree, G. Swapna, R.J. Martis and J.S. Suri "Automated EEG analysis of epilepsy: A review", *Knowledge Based Systems*, vol. 45, pp.147 -165, 2013
[31] A. T. Tzallas, M. G. Tsipouras, D. G. Tsalikakis, E. C. Karvounis, L. Astrakas, S. Konitsiotis and M. Tzaphlidou"Automated epileptic seizure detection methods: A review study", *Epilepsy-Historical, Electroencephelographic and Psychological Aspects*, pp.75 -98, 2012
[32] S. Altunay, Z. Telatar, and O. Erogul, "Epileptic EEG detection using the linear prediction error energy," *Expert Syst. Appl*., vol. 37, no. 8, pp. 5661-5665, 2010.
[33] V. Joshi, R.B. Pachori, and A. Vijesh, "Classification of ictal and seizure free EEG signals using fractional linear prediction," *Biomed. Signal Proces*, vol. 9, pp. 1-5, 2014.
[34] S. Ghosh-Dastidar , H. Adeli and N. Dadmehr "Principal component analysis-enhanced cosine radial basis function neural network for robust epilepsy and seizure detection", *IEEE Trans. Biomed. Eng*., vol. 55, no. 2, pp.512 -518, 2008
[35] T.S. Kumar, V. Kanhangad and R.B. Pachori "Classification of seizure and seizure-free EEG signals using local binary patterns", *Biomed. Signal Proces*, vol. 15, pp.33 -40, 2015
[36] A.T. Tzallas, M.G. Tsipouras and D.I. Fotiadis "Epileptic seizure detection in EEGs using time–frequency analysis", *IEEE Trans. Inf. Technol. Biomed*., vol. 13, no. 5, pp.703 -710, 2009
[37] U.R. Acharya, R. Yanti, J.W. Zheng, M.R. Krishnan, J.H. Tan, R.J. Martis, and C.M. Lim, "Automated diagnosis of epilepsy using CWT, HOS and texture parameters", *Int J Neural Syst*, vol. 23, no. 3, pp.1350009, 15 pages, 2013.
[38] A. Subasi and M.I. Gursoy "EEG signal classification using PCA, ICA, LDA and support vector machines", *Expert Syst. Appl*., vol. 37, no. 12, pp.8659 -8666, 2010
[39] R. Uthayakumar and D. Easwaramoorthy, "Epileptic seizure detection in EEG signals using multifractal analysis and wavelet transform," *Fractals*, vol. 21, no. 2, 2013.
[40] R. Sharma and R.B. Pachori, "Classification of epileptic seizures in EEG signals based on phase space representation of intrinsic mode functions," *Expert Syst. Appl*., vol. 42, no. 3, pp. 1106-1117, 2015.
[41] R.B. Pachori and S. Patidar, "Epileptic seizure classification in EEG signals using second-order difference plot of intrinsic mode function," *Comput. Methods Prog. Biomed*., vol. 113, issue 2, pp. 494-502, 2014.
[42] V. Bajaj and R.B. Pachori, "Classification of seizure and nonseizure EEG signals using empirical mode decomposition*," IEEE Trans. Inf. Technol. Biomed*., vol. 16, no. 6, pp. 1135-1142, 2012.
[43] R.B. Pachori and V. Bajaj "Analysis of normal and epileptic seizure EEG signals using empirical mode decomposition", *Comput. Methods Progr. Biomed*., vol. 104, no. 3, pp.373 -381, 2011
[44] V. Bajaj and R.B. Pachori, "Epileptic seizure detection based on the instantaneous area of analytic intrinsic mode functions of EEG signals*," Biomed Eng Lett.*, vol. 3, no. 1, pp 17-21, 2013.
[45] R.B. Pachori, R. Sharma, and S. Patidar. "Classification of normal and epileptic seizure EEG signals based on empirical mode decomposition" *in Complex System Modelling And Control Through Intelligent Soft Computations Studies In Fuzziness And Soft Computing*, 1st ed. Springer International Publishing, pp. 367–388, 2015.
[46] U.R. Acharya, S.V. Sree, S. Chattopadhyay, W. Yu and P.C. Ang, "Application of recurrence quantification analysis for the automated identification of epileptic EEG signals", *Int J Neural Syst.*, 21 (3): 199-211, 2011.
[47] U.R. Acharya, C.K. Chua, T.-C. Lim, Dorithy and J.S. Suri "Automatic identification of epileptic EEG signals using nonlinear parameters*", J Mech. Med. Biol.*, vol. 9, pp. 539–553, 2009
[48] U.R. Acharya, S.V. Sree and J.S. Suri "Automatic detection of epileptic EEG signals using higher order cumulant features", *Int. J. Neural Syst.*, vol. 21, no. 5, pp.403 -414, 2011
[49] V. Srinivasan , C. Eswaran and N. Sriraam "Approximate entropy-based epileptic EEG detection using artificial neural networks", *IEEE Trans. Inf. Technol. Biomed*., vol. 11, no. 3, pp.288 -295, 2007.
[50] S. Chaudhuri, S. Chatterjee, N. Katz, M. Nelson, and M. Goldbaum, "Detection of blood vessels in retinal images using two-dimensional matched filters," *IEEE Trans. Med. Imag*., vol. 25, pp. 203–210, 1989.
[51] R.O. Duda, P.E. Hart, and D.G. Stork, *Pattern Classification*. John Wiley & Sons, 2001.
[52] M. K. Hu, "Visual pattern recognition by moment invariants," *IRE Trans. Inform. Theory*, vol. 8, pp. 179–187, 1962.
[53] P.H. Gregson, Z. Shen, R.C. Scott, and V. Kozousek, "Automated grading of venous beading," *Computers and Biomedical Research*, vol. 28, pp. 291–304, 1995.
[54] D. Lowe, "Distinctive Image Features from Scale-Invariant Keypoints," *Int',l J. Computer Vision*, vol. 2, no. 60, pp. 91-110, 2004.
[55] Y. Zhang, G. Pan, K. Jia, M. Lu, Y. Wang, Z. Wu "Accelerometer-based gait recognition by sparse representation of signature points with clusters", *IEEE Trans. Cybern.*, vol. 45, no. 9, pp.1864 -1875, 2015
[56] M. Heikkila, M. Pietikainen and C. Schmid "Description of interest regions with local binary patterns", *Pattern Recog*., vol. 42, no. 3, pp.425 -436, 2009.
[57] C. Cortes and V. Vapnik, "Support-vector network", *Machine Learning*, vol. 20, pp.273 -297, 1995.
[58] M. Hall, E. Frank, G. Holmes, B. Pfahringer, P. Reutemann, and I. Witten "The WEKA data mining software: An update", *ACM SIGKDD Explorations Newsletter*, vol. 11, no. 1, pp. 10-18, 2009.
[59] A. Hoover, V. Kouznetsova, and M. Goldbaum, "Locating blood vessels in retinal images by piecewise threshold probing of a matched filter response," *IEEE Trans. Med. Imag*., vol. 19, pp. 203–210, Mar. 2000.
[60] P.Bankhead, C.N.Scholfield, J.G.McGeown, and T.M.Curtis, "Fast retinal vessel detection and measurement using wavelets and edge location refinement," PLOS ONE, vol.7, no.3, Jan.2012.
[61] A. Salazar-Gonzalez, D.l Kaba, Y. Li and X. Liu., "Segmentation of blood vessels and optic disc in retinal images", *IEEE J. Biomed. Health Informat*., vol. 18, no. 6, pp. 1874-1886, Jan 2014.
[62] R. Annunziata, A. Garzelli, L. Ballerini, and A. Mecocci, "Leveraging multiscale hessian-based enhancement with a novel exudate inpainting technique for retinal vessel segmentation," *IEEE J. Biomed. Health Informat*., June 2015. (In press)
[63] B. S. Y. Lam, G. Yongsheng and A. W. C. Liew "General retinal vessel segmentation using regularization-based multiconcavity modeling*", IEEE Trans. Med. Imaging*, vol. 29, no. 7, pp. 1369 -1381, 2010.
[64] K. A. Vermeer, F. M. Vos, H. G. Lemij, and A. M. Vossepoel, "A model based method for retinal blood vessel detection," *Comput. Biol. Med*., vol. 34, no. 3, pp. 209–219, 2004.
[65] B. Al-Diri, A. Hunter, D. Steel, M. Habib, T. Hudaib, and S. Berry, "Review—A reference data set for retinal vessel profiles," *in Proc. 30th Annu. Int. Conf. IEEE Eng. Med. Biol. Soc*., Aug. 2008, pp. 2262–2265.
[66] X. Xu, M. Niemeijer, Q. Song, M. Sonka, M. K. Garvin, J. M. Reinhardt, and M. D. Abramoff, "Vessel boundary delineation on fundus images using graph-based approach," *IEEE Transactions on Medical Imaging*, vol. 30, no. 6, pp. 1184–1191, 2011.

[67] P.H. Gregson, Z. Shen, R.C. Scott, and V. Kozousek, "Automated grading of venous beading," *Computers and Biomedical Research*, vol. 28, pp. 291–304, 1995.
[68] O. Brinchmann-Hansen and H. Heier, "Theoretical relations between light streak characteristics and optical properties of retinal vessels," *Acta Ophthalmologica*, supplement, vol. 179, pp. 33–37, 1986.
[69] L. Zhou, M. S. Rzeszotarski, L. J. Singerman, and J. M. Chokreff, "The detection and quantification of retinopathy using digital angiograms," *IEEE Transactions on Medical Imaging*, vol. 13, no. 4, pp. 619–626, 1994.
[70] J. Lowell, A. Hunter, D. Steel, A. Basu, R. Ryder, and R. Kennedy, "Measurement of retinal vessel widths from fundus images based on 2-D modeling," *IEEE Transactions on Medical Imaging*, vol. 23, no. 10, pp. 1196–1204, October 2004.
[71] R.G. Andrzejak, K. Lehnertz, F. Mormann, C. Rieke, P. David, and C.E. Elger, "Indications of nonlinear deterministic and finite-dimensional structures in time series of brain electrical activity: Dependence on recording region and brain state," *Phys. Rev. E*, vol. 64, 061907, 2001. [Online] Available: http://www.meb.unibonn.de/epileptologie/science/physik/eegdata.html
[72] T. Gandhi, B.K. Panigrahi, M. Bhatia, S. Anand, "Expert model for detection of epileptic activity in EEG signature," *Expert Syst. Appl.*, vol. 37, pp. 3513-3520, 2010.
[73] B.W. Matthews, "Comparison of the Predicted and Observed Secondary Structure of T4 Phage Lysozyme," *Biochimica et Biophysics Acta*, vol. 405, pp. 442-451, Oct. 1975.
[74] M. Peker, B. Sen and D. Delen, "A novel method for automated diagnosis of epilepsy using complex-valued classifiers", *IEEE J Biomed Health Inform.*, 2015. (In press)
[75] K. Fu, J. Qu, Y. Chai, and Y. Dong, "Classification of seizure based on the time-frequency image of EEG signals using HHT and SVM", *Biomed. Signal Process. Control*, vol. l3, pp.15-22, 2014.
[76] K. Samiee, P. Kovacs, M. Gabbouj, "Epileptic seizure classification of EEG time-series using rational discrete short-time fourier transform*", IEEE Trans. Biomed. Eng.*, vol. 62, no. 2, pp.541-552, 2015.
[77] M.Z. Parvez, M. Paul, "Epileptic seizure prediction by exploiting spatiotemporal relationship of EEG signals using phase correlation" *IEEE Trans. Neural Syst. Rehabil. Eng.*, 2015 (In press)
[78] G. Chen, "Automatic EEG seizure detection using dual-tree complex wavelet-Fourier features," *Expert system with applications*, vol 41, pp.2391-2394, 2014.
[79] L. Guo, D. Rivero and A. Pizos "Epileptic seizure detection using multiwavelet transform based approximate entropy and artificial neural networks", *J. Neurosci. Methods*, vol. 193, no. 1, pp.156 -163, 2010
[80] L. Guo, D. Rivero, J. Dorado, C.R. Munteanu and A. Pazos, "Automatic feature extraction using genetic programming: An application to epileptic EEG classification", *Expert Syst. Appl.*, vol.38, no.8, pp.10425-10436, 2011.
[81] Z. Iscan, Z. Dokur and T. Demilrap, "Using Classification of electroencephalogram signals with combined time and frequency features*", International Journal of Expert Syst. Appl.*, vol. 38, pp. 10499-10505, 2011.
[82] A. Lima, A.L. Coelho and M. Eisencraft "Tackling EEG signal classification with least squares support vector machines: a sensitivity analysis study", *Comput. Biol. Med.*, vol. 40, no. 8, pp.705 -714, 2010
[83] U. Orhan, M. Hekim, and M. Ozer. "EEG signals classification using the K-means clustering and a multilayer perceptron neural network model," *Expert Syst. Appl.*, Vol. 38, pp. 13475-13481, 2011
[84] A.T. Tzallas, M.G. Tsipouras and D.I. Fotiadis "Automatic seizure detection based on time-frequency analysis and artificial neural networks*", Comput. Intell. Neurosci.*, vol. 2007, pp.80510-1 -80510-13, 2007
[85] E.D. Übeyli, "Least squares support vector machine employing model-based methods coefficients for analysis of EEG signals", *Expert Syst. Appl.*, vol. 37, no. 1, pp.233 -239, 2010
[86] D. Wang, D.Q. Miao and C. Xie,"Best basis-based wavelet packet entropy feature extraction and hierarchical EEG classification for epileptic detection", *Expert Syst. Appl.*, vol. 38, no. 11, pp.14314 -14320, 2011
[87] U.R. Acharya, S.V. Sree, A.P. Alvin, R. Yantiand J.S. Suri, "Application of non-linear and wavelet based features for the automated identification of epileptic EEG signals", *Int J Neural Syst*, vol. 22, no. 2, pp. 1-14, 2012.
[88] U.R. Acharya, F. Molinari, S.V. Sree, S. Chattopadhyay, Ng. Kwang-Hoong, J.S. Suri, "Automated diagnosis of epileptic EEG using entropies", *Biomed. Signal Proces*, vol. 7, no. 4, pp. 401-408, 2012.
[89] U.R. Acharya, S.V. Sree, A.P.C. Alvin and J.S. Suri, "Use of principal component analysis for automatic classification of epileptic EEG activities in wavelet framework", *Expert Syst. Appl.*, vol. 39, no. 10, pp. 9072-9078, 2012.
[90] K.C. Chua, V. Chandran, U.R. Acharya, C.M. Lim, "Application of higher order spectra to identify epileptic EEG", *J. Med. Syst.*, vol. 35, pp.1563 -1571, 2011
[91] O. Faust, U.R. Acharya, L.C. Min, and B.H. Sputh, "Automatic identification of epileptic and background EEG signals using frequency domain parameters," *Int J Neural Syst*, vol. 20, no. 2, pp. 159-176, Apr, 2010.
[92] L. Guo, D. Rivero, J. Dorado , J.R. Rabuñal and A. Pazos "Automatic epileptic seizure detection in EEGs based on line length feature and artificial neural networks*", J. Neurosci. Methods*, vol. 191, pp.101 -109, 2010
[93] H. Ocak "Automatic detection of epileptic seizures in EEG using discrete wavelet transform and approximate entropy", *Expert Syst. Appl.*, vol. 36, pp.2027 -2036, 2009